Computers and Geotechnics 84 (2017) 28–46

Contents lists available at ScienceDirect

Computers and Geotechnics

journal homepage: www.elsevier.com/locate/compgeo

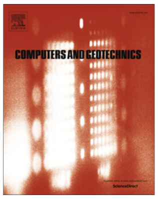

Research Paper

A constitutive mechanical model for gas hydrate bearing sediments incorporating inelastic mechanisms

Marcelo Sánchez[a,*], Xuerui Gai[a], J. Carlos Santamarina[b]

[a] Zachry Department of Civil Engineering, Texas A&M University, College Station, USA
[b] Earth Science & Engineering, King Abdullah University of Science and Technology, Saudi Arabia

ARTICLE INFO

Article history:
Received 30 January 2016
Received in revised form 17 September 2016
Accepted 20 November 2016

Keywords:
Methane hydrate
Geomechanical behavior
Damage
Elastoplasticity
Model application

ABSTRACT

Gas hydrate bearing sediments (HBS) are natural soils formed in permafrost and sub-marine settings where the temperature and pressure conditions are such that gas hydrates are stable. If these conditions shift from the hydrate stability zone, hydrates dissociate and move from the solid to the gas phase. Hydrate dissociation is accompanied by significant changes in sediment structure and strongly affects its mechanical behavior (e.g., sediment stiffenss, strength and dilatancy). The mechanical behavior of HBS is very complex and its modeling poses great challenges. This paper presents a new geomechanical model for hydrate bearing sediments. The model incorporates the concept of partition stress, plus a number of inelastic mechanisms proposed to capture the complex behavior of this type of soil. This constitutive model is especially well suited to simulate the behavior of HBS upon dissociation. The model was applied and validated against experimental data from triaxial and oedometric tests conducted on manufactured and natural specimens involving different hydrate saturation, hydrate morphology, and confinement conditions. Particular attention was paid to model the HBS behavior during hydrate dissociation under loading. The model performance was highly satisfactory in all the cases studied. It managed to properly capture the main features of HBS mechanical behavior and it also assisted to interpret the behavior of this type of sediment under different loading and hydrate conditions.

1. Introduction

Gas hydrate bearing sediments (HBS) are naturally occurring soils characterized by the presence of ice like gas (e.g., CH_4 or CO_2) hydrates in its pore space. Water molecules clustered around methane molecules form a solid compound called methane hydrate that are naturally found in marine sediments and permafrost regions, where the (high) pressure and (low) temperature conditions guarantee the hydrates stability [1–3]. Perturbations in pressure, temperature or water-chemistry may move the methane hydrates from its stability zone triggering hydrate dissociation. Hydrate dissociation is accompanied by gas and water production, as well as, by significant changes in the sediment structure and mechanical properties. The amount of hydrate in soils is commonly evaluated by means of the hydrate saturation (S_h), calculated as the ratio between the volume occupied by the hydrates and the volume of voids.

HBS represents an attractive source of energy, it is estimated that significant methane reserves are in the form of hydrates. However, HBS are also associated with a number of issues and drawbacks. For example, massive submarine landslides are in occasions related to hydrate dissociation from subsea sediments. This type of phenomenon generally involves large areas and may affect pipelines and other submarine infrastructure. A number of engineering problems (e.g., blowouts; platform foundation failures; and borehole instability) are sometimes triggered by hydrate dissociation. Furthermore, the venting of methane to the atmosphere during uncontrolled hydrate dissociation can negatively contribute to greenhouse effects [4].

Geomechanics is a key component in the numerical modeling of engineering problems involving HBS. Several types of mechanical constitutive models for hydrate bearing sediment have been proposed in the last few years [5–23]. Only a few of them are discussed below. For example, Miyazaki et al. [5] suggested a nonlinear elastic model for hydrate bearing sands based on the Duncan-Chang model (e.g., [24]). The Mohr–Coulomb (MC) model has been adopted by several researchers to describe the behavior of HBS. For instance, Rutqvist and Moridis [8] simulated the geomechanical changes during gas production from HBS undergoing depressurization-induced dissociation using a modified MC model. Klar et al. [7] proposed a single-phase elastic–perfectly plastic MC model for hydrate soils based on the concept of effective stress that incorporates an

---

* Corresponding author at: Zachry Department of Civil Engineering, Texas A&M University, College Station, TX 77843-3136, USA.

E-mail address: msanchez@civil.tamu.edu (M. Sánchez).

http://dx.doi.org/10.1016/j.compgeo.2016.11.012

enhanced dilation mechanism. Pinkert and Grozic [9,10] proposed a model based on a non-linear elastic model (dependent on S_h) and the on MC failure criterion. This model was able to fit well Miyazaki et al. [25] experimental data. This model was used to simulate wellbore stability problems and accounted for the effect of S_h on mechanical strength and stiffness. The extension of MC type models to deal with hydrates is generally carried out by incorporating a dependency of the cohesion with the hydrate concentration (i.e., [7–9]). However, Pinkert [26] showed that by using the Rowe's stress-dilatancy theory [27], it was possible to model the behavior of hydrates without the need of enhancing the cohesion with the increase of S_h. As it is well-known, MC type models cannot capture plastic deformations before failure and are unable to simulate positive (compressive) plastic deformations.

The model based on the Modified Cam-Clay (MCC) framework proposed by Sultan and Garziglia [13] was validated against the experimental data reported by Masui et al. [28,29]. This model was calibrated against experimental data gathered from triaxial tests on synthetic hydrate sediments [29]. The global performance of the model was satisfactory, however, it was unable to capture the softening behavior observed in these experiments. The critical state model for HBS proposed by Uchida et al. [14,15] is based on the MCC model and its validation was performed using published experiments conducted at constant hydrate saturation. Lin et al. [11] developed a critical state model based on the 'spatial mobilized plane' framework and sub-loading concepts. The performance of this model was satisfactory when compared against triaxial test data from laboratory-synthesized samples and also from field specimens extracted from Nankai Trough, Japan [28,29]. Kimoto et al. [6] proposed an elasto–viscoplastic model to analyze ground deformations induced by hydrate dissociation. The discrete element method has also been used to simulate the mechanical behavior of HBS (e.g., [17–19,21–23]). All the mechanical models discussed above have been used to simulate tests performed at constant hydrate saturation.

In this study a new elasto-plastic model based on the stress partition concept [30–33] and the HIerarchical Single Surface (HISS) framework (e.g., [34–36]) was selected to provide a general and adaptable geomechanical model for hydrate bearing sediments. Recently published experimental data based on synthetic and natural specimens involving different S_h and hydrates morphology was adopted to validate the proposed approach. The model application and validation do not limit to cases in which S_h is maintained constant during the tests (as in previous works), but also include experiments in which dissociation is induced under constant stress. Particular attention is paid to evaluate the behavior of HBS during dissociation under different stress levels and tests conditions (i.e., triaxial and oedometric), as well as experiments involving both: reconstituted and natural specimens. The model also allows examining the individual contribution of sediments and hydrates to the mechanical behavior during loading and dissociation, aspect that was not studied before with an elastoplastic model for HBS.

In the following section the mechanical behavior of HBS is briefly discussed to provide some background information about the key features of this material. The main components of the adopted elasto-plastic framework are presented afterwards. Then, the application and validation cases selected to study the behavior of HBS are discussed. Finally, the main conclusions of the work are summarized.

2. Mechanical behavior of HBS - experimental evidences

In the following sections experimental evidences related to the mechanical behavior of HBS are briefly discussed.

2.1. Loading tests at constant hydrate saturation

Triaxial tests at constant hydrate saturation have provided very useful information to understand the influence of hydrate saturation and morphology on the mechanical behavior of HBS. The presence of hydrates strongly affects key mechanical properties of soils. Gas hydrate increases the shear strength of the sediment [25,28]. Hydrates specimens exhibit a softening behavior (after the peak stress) and more dilation than free hydrate samples [25,28]. The sediment stiffness and strength generally increase with the increase in hydrate saturation [25,28]. It has also been observed that the stiffness of HBS degrades during shearing [29,37–43].

Hydrates are generally present in sediments in three main morphology types [44,45]: (a) cementation (Fig. 1a); (b) pore-filling (Fig. 1b); and (c) load-bearing (Fig. 1c).

Hydrates formed in the cementation mode are typically found at the contact between particles. A recent microstructural investigation [57] (that does not involve any mechanical test), speculates about the actual cementation effects provided by the hydrates. However a large number of studies support that hydrates formed in the cementing mode do provide bonding between soil particles [11,14,15,17–23,26,29,45–47,49,64]. For this morphology type, even a small hydrate saturation can significantly contribute to increase the sediment stiffness and strength [49]. In hydrate morphology type (b), the hydrates nucleate on soil grains boundaries and grow freely into the pore space, without bridging two or more particles together. This type of hydrates also impacts on the mechanical properties of the sediments. When hydrate saturation is above 25%, this morphology turns into the load-bearing type (c) [50–52]. Sediment permeability and water storage capacity are significantly affected by the presence of hydrates in the load-bearing form [53]. This mode is generally found in fine-grained soils and a typical example is the Mallik 5L-38 sediment [54].

Fig. 2a presents some typical results showing the effect of S_h on stress-strain behavior and strain-volumetric response of natural methane hydrate samples under triaxial conditions [28]. The type of hydrate pore-habit (i.e., morphology) also affects sediment behavior. For example, the tests conducted by Masui et al. [29] to study the influence of hydrate morphology on the geomechanical response of hydrate bearing sediments are shown in Fig. 2b. Of the three samples investigated in that research, the sample without hydrates (i.e., pure sediment) exhibited lower stiffenss, strength, and dilatancy. The presence of hydrates increases the material stiffenss, strength and dilatancy, corresponding the maximum values to the cementing mode (i.e., type 'a', above).

2.2. Hydrate dissociation tests under load

Hydrate dissociation experiments under stress have allowed gaining a better understanding on the mechanical response of sediments when the presence of hydrates vanish or partially disappear. Two types of tests involving hydrate dissociation conducted under triaxial and oedemetric loading conditions are briefly discussed in this section.

Hyodo et al. [37] adopted a temperature-controlled high pressure triaxial apparatus to mimic the formation and dissociation of methane hydrate in the deep seabed. This device was used to conduct a series of triaxial compression tests on synthetic HBS samples under various stress conditions. Toyoura sand was chosen as the host material to prepare samples with a similar porosity (i.e., ~40%), and with S_h ranging from ~37% to ~53%. Firstly, water and sand were mixed to form the specimen at the target density [37]. The sample was placed in a freezer to keep it stand and then in a triaxial cell, at the target pressure and room temperature [37]. Once the specimen was thawed, methane was injected into the specimen, while keeping the cell pressure and temperature condi-

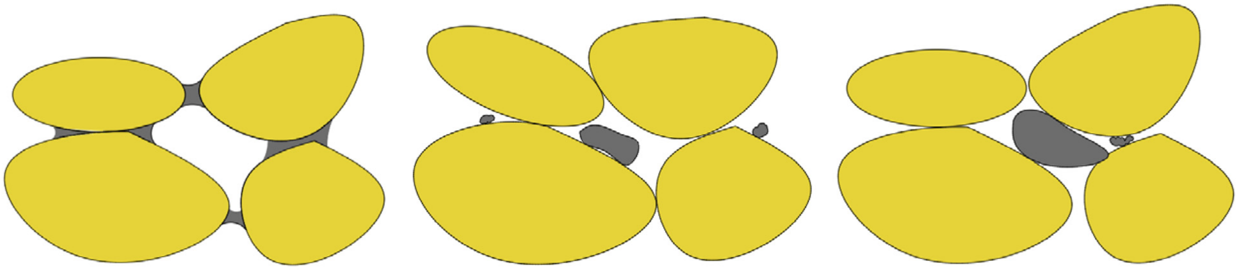

a) cementation b) pore filling c) supporting matrix

Fig. 1. Main types of hydrate morphology: (a) cementation; (b) pore-filling; and (c) load-bearing.

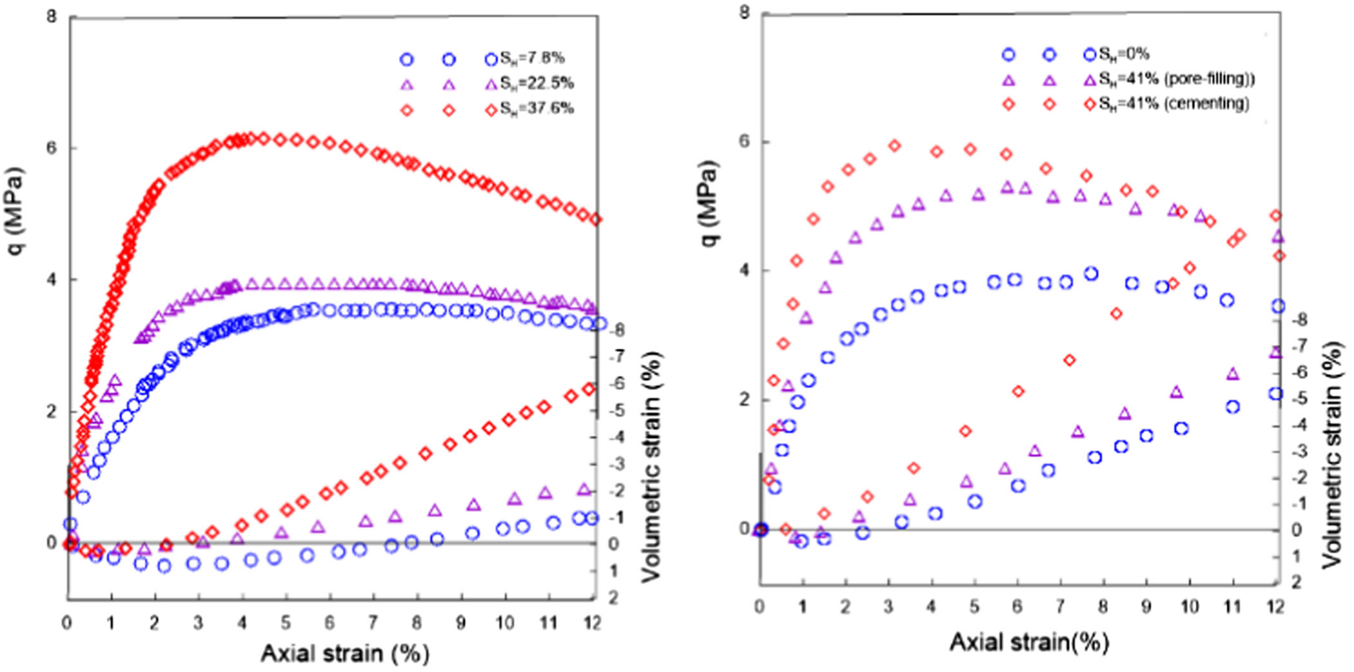

(a) (b)

Fig. 2. Tests on natural and synthetic HBS in terms of stress-strain behavior and volumetric response (a) specimens prepared at different hydrate saturation and (b) samples prepared with different hydrate morphology [28,29].

tion inside the hydrate stability zone [37]. Three experiments were selected in this work for the numerical simulations (see Section 4.4), namely: two triaxial tests at which hydrate dissociation was induced at two different initial axial strains (i.e., $\varepsilon_a = 1\%$ and $\varepsilon_a = 5\%$), and a third one in which the sample was subjected to shearing after the hydrates dissociated completely. These tests were conducted under isotropically consolidated specimens, at an effective confining stress $\sigma'_c = 5$ MPa under drained conditions. Fig. 3a presents the main experimental results in terms of axial strains against both deviatoric stress and volumetric strains. In one of the hydrate dissociation tests, the specimen was firstly sheared up to $q \approx 8.4$ MPa (i.e., at $\varepsilon_a = 1\%$), then hydrate dissociation was induced at constant stress conditions and, once hydrate dissociation was completed, but the shearing continued up to $\varepsilon_a = 20\%$. A similar procedure was followed for the other test, but the maximum deviatoric load in this cases was $q \approx 12$ MPa (i.e., at $\varepsilon_a = 5\%$). The responses observed under these tests conditions are quite different. In the first test, the deviatoric stress after hydrate dissociation was smaller than the shear strength of the dissociated sediment, therefore a tendency to harden was observed in the subsequent shearing. However, in the second sample (i.e., dissociation induced at $\varepsilon_a = 5\%$) the deviatoric stress was higher than the strength of the dissociated sample. In consequence, a stress-softening behavior was observed during the hydrate dissociation stage, with a tendency of the deviatoric stress to decrease until reaching the maximum deviatoric stress observed in the already dissociated sample. More details about these tests and the associated modeling are presented in Section 4.4.

The other set of experiments modeled in this paper corresponds to the tests reported by Santamarina et al. [55]. Two natural core samples were extracted from the Nankai Trough, offshore Japan, using the Pressure Core Characterization Tools (PCCT [56]). The tested cores were predominantly sandy- and clayey-silts, but also contained some silty-sands. Hydrate saturation ranged from ~15% to ~74%, with significant concentrations in the silty-sands samples. The PCCT was able to maintain the HBS cores stable at field conditions. After retrieval, the cores were loaded under oedometric conditions and at some point, hydrate dissociation was induced under constant effective stress conditions. The mechanical behavior of the HBS specimens before, during and after dissociation was recorded. Fig. 3b shows the results of a typical test in the 'effective stress chamber' (i.e., the sample coded as 'core-10P', with an initial

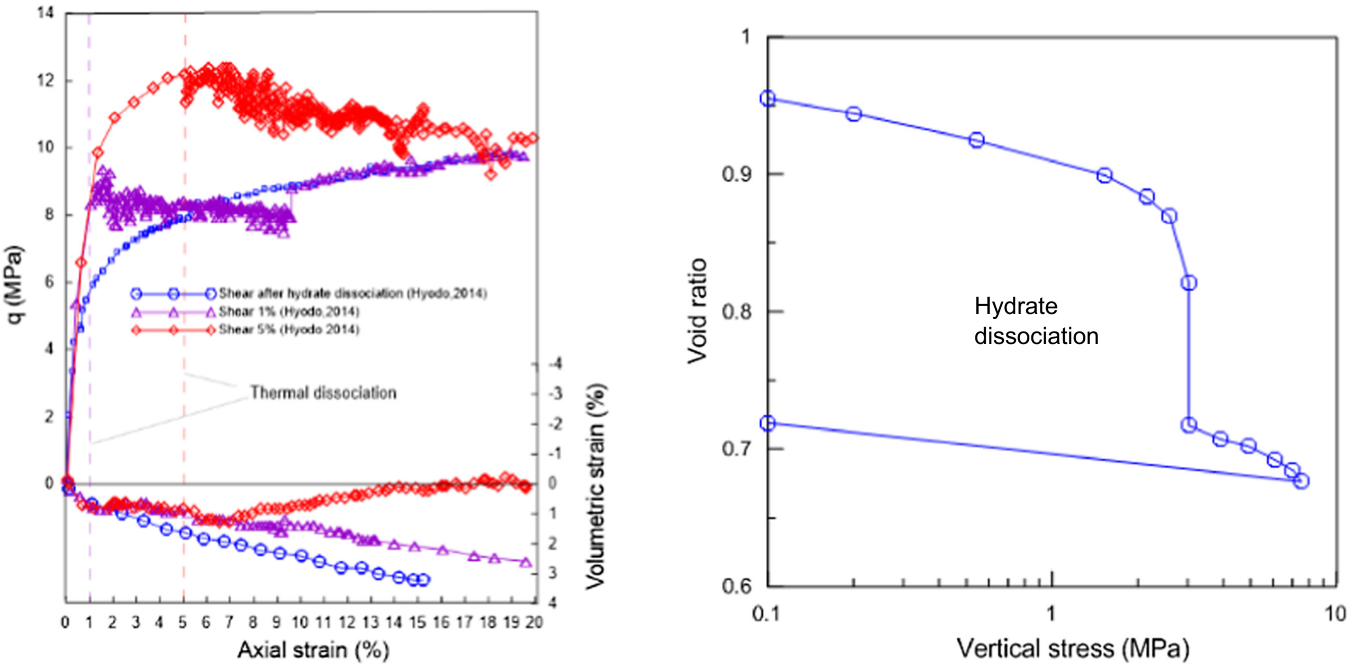

(a) (b)

Fig. 3. (a) Experimental results for drained triaxial tests involving hydrate dissociation [37] and (b) behavior of a natural HBS subjected to loading and dissociation under stress at oedemetric conditions [55].

$S_h \sim 74\%$ [55]). Prior to hydrate dissociation, the specimen was loaded up to an applied effective vertical stress $\sigma'_v = 3$ MPa, then hydrate dissociation was induced via depressurization, maintaining the effective stress constant. Once the hydrates were fully dissociated, the specimen was loaded up to $\sigma'_v = 9$ MPa, and it was unloaded afterwards. A significant volumetric collapse-compression deformation was observed during dissociation under load. This test and another one with lower hydrate dissociation (i.e., $S_h \sim 18\%$) are modeled and discussed in Section 4.6.

2.3. Discussion

The mechanical behavior of HBS is highly complex because its response not only depends on the amount of hydrate, but also on the type of pore habit (i.e., cementing, pore-filling, or load-bearing s). It was observed that the behavior of HBS during hydrate dissociation (and after it) depends on stress level, as shown in more detail in Section 4.4. It has also been suggested that hydrate bonding effects can be damaged during shearing [11,14,15]. The progressive stiffness degradation in tests involving HBS is generally very evident. Fig. 4a illustrates the phenomenon of hydrate damage during shearing. Hydrate dissociation is also accompanied by profound changes in the sediment structure. Fig. 4b shows schematically the expected changes in the soil structure that lead to the collapse compression deformations observed during dissociation under normally consolidated conditions (e.g., Fig. 3b). In summary, the mechanical response of HBS is highly non-linear, controlled by multiple inelastic phenomena that depends on hydrate saturation, sediment structure, and stress level. In the following section, an advanced elastoplastic model for HBS is presented in detail.

3. Model description

The stress-partition concept proposed by Pinyol Puigmartí et al. [32] for clayed cementing materials is adapted in this work for describing the behavior of HBS. The main reason behind the selection of this model is that it is extremely well suited to deal with materials that have two main constituents (i.e., 'hydrates' and 'sediments' in this case), feature that is not considered in previous models for HBS. The model allows to explicitly define specific constitutive models and evolutions laws for each one of those two compounds with the corresponding variables. The modeling of the hydrates can be well represented by a damage model that is able to account for the material degradation induced by loading and hydrate dissociation. As for the sediment skeleton, a model based on critical state soil mechanics concepts is adopted, which is an appropriate approach for describing the elastoplastic behavior of the soils. The particular constitutive equations adopted hereafter are based on a modification of the HISS elasto-plastic model [34–36]. The proposed framework also incorporates sub-loading and dilation enhancement concepts.

Therefore, the proposed model takes in account two basic aspects related to the presence of hydrates in soils: (i) it considers that hydrates contribute (together with the soil skeleton) to the mechanical stability of the sediment, the stress partition concept is used to compute this contribution; and (ii) it contemplates that the presence of hydrates alters the mechanical behavior of sediments (e.g., providing hardening and dilation enhancement effects), inelastic mechanisms are incorporated into a critical state model for the sediment to account for these effects.

The main model components and its mathematical formulation are detailed below, introducing firstly some basic relationships, detailing afterwards the specific constitutive models for the hydrates and sediment, and developing finally the global stress-strain equations.

3.1. Basic relationships

The stress-partition concept [32] was adopted to develop the basic relationships. The total volume of the sample (V) can be computed as:

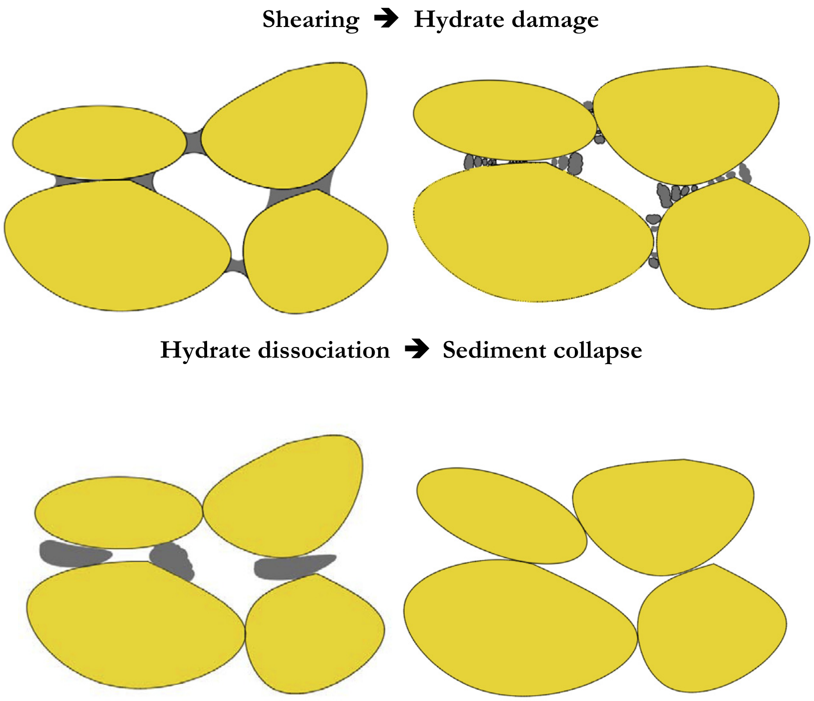

Fig. 4. (a) Schematic representation of the hydrate damaged during shearing and (b) rearrangement of the HBS structure upon dissociation.

$$V = V_s + V_h + V_f \tag{1}$$

where V_s is the volume of sediment skeleton, V_h is the volume of hydrate, V_f is the volume occupied by the fluid in the pore space (Fig. 5).

Assuming that the soil grains are incompressible, the total volumetric strain can be defined as:

$$\varepsilon^v = -\frac{\Delta V_f}{V} - \frac{\Delta V_h}{V} \tag{2}$$

where the superscript v indicates volumetric strains. The volumetric strain of methane hydrate is computed as:

$$\varepsilon_h^v = -\frac{\Delta V_h}{V_h} \tag{3}$$

The deformation of hydrate can be defined locally through the following relationship:

$$-\frac{\Delta V_h}{V} = -\frac{\Delta V_h}{V_h}\frac{V_h}{V} = \varepsilon_h^v C_h \tag{4}$$

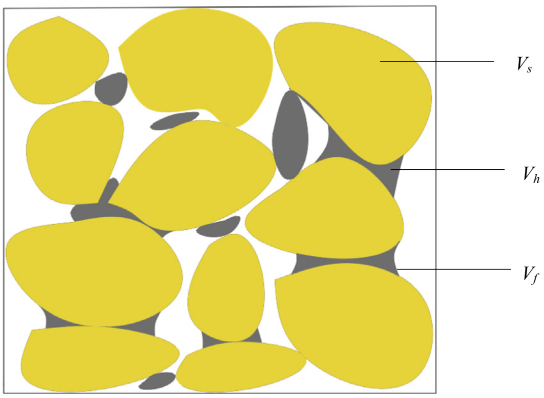

Fig. 5. Schematic representation of a HBS.

where C_h is the volumetric concentration of methane hydrate; which in turns is equal to the porosity (ϕ) times the hydrate saturation (i.e., $C_h = \phi\ S_h$). From Eqs. (2) and (4), the total volumetric strain accounting for both the sediment skeleton (i.e., subscript *ss*) and the hydrates deformations can be calculated as:

$$\varepsilon^v = \varepsilon_{ss}^v + C_h \varepsilon_h^v \tag{5}$$

In a similar fashion, the deviatoric strains can be computed as:

$$\varepsilon^q = \varepsilon_{ss}^q + C_h \varepsilon_h^q \tag{6}$$

The relationships that link hydrates and soil skeleton strains are proposed following an approach similar to [32]:

$$\varepsilon_h^v = \chi \varepsilon_{ss}^v \tag{7}$$

$$\varepsilon_h^q = \chi \varepsilon_{ss}^q \tag{8}$$

where χ is the strain partition variable that evolves during loading. The evolution law for this variable is presented in Section 3.2. From these equations, it can be anticipated that when the sediment skeleton deforms, the local hydrate strain reduces if χ decreases. Combining Eqs. (5)–(8) leads to:

$$\varepsilon_h^v = \frac{\chi}{1 + C_h \chi}\varepsilon^v \tag{9}$$

$$\varepsilon_h^q = \frac{\chi}{1 + C_h \chi}\varepsilon^q \tag{10}$$

Eqs. (9) and (10) can also be written as a vector:

$$\boldsymbol{\varepsilon}_h = \frac{\chi}{1 + C_h \chi}\boldsymbol{\varepsilon} \tag{11}$$

In the following sections the specific constitutive models for the hydrate and sediment skeleton are discussed.

3.2. Constitutive model for the methane hydrate

The damage theory is an appropriate framework to describe the degradation process of geomaterials subjected to loading [58]. Isotropic scalar damage models track the degradation behavior of materials via damage variables. Loading degradation occurs when the stress state arrives to a predefined threshold. As mentioned above, previous studies suggested that hydrate can be damaged during shearing [11,14,15]. It is also assumed here that the material degradation takes place during hydrate dissociation. When the stresses are below a pre-established threshold, a linear elastic response of the material is assumed via the following relationships:

$$\boldsymbol{\sigma}_h = \mathbf{D}_{h0}\boldsymbol{\varepsilon}_h \tag{12}$$

where $\boldsymbol{\sigma}_h$ corresponds to the stresses taken by the hydrate and $\mathbf{D}_{h0}$ is the methane hydrate elastic constitutive matrix of the intact material, as follows:

$$\mathbf{D}_{h0} = \begin{bmatrix} K_{h0} + \frac{4}{3}G_{h0} & K_{h0} - \frac{2}{3}G_{h0} & K_{h0} - \frac{2}{3}G_{h0} & 0 & 0 & 0 \\ & K_{h0} + \frac{4}{3}G_{h0} & K_{h0} - \frac{2}{3}G_{h0} & 0 & 0 & 0 \\ & & K_{h0} + \frac{4}{3}G_{h0} & 0 & 0 & 0 \\ & \mathit{Symetric} & & G_{h0} & 0 & 0 \\ & & & & G_{h0} & 0 \\ & & & & & G_{h0} \end{bmatrix} \tag{13}$$

where K_{h0} and G_{h0} are the bulk and shear moduli, of the intact hydrate, respectively. A logarithmic isotropic damage variable (L: $+\infty > L \geqslant 0$) is introduced to account for the damage induce by loading [31]. The following expressions can be adopted for damaged states:

$$\boldsymbol{\sigma}_h = e^{-L}\mathbf{D}_{h0}\boldsymbol{\varepsilon}_h = \mathbf{D}_h\boldsymbol{\varepsilon}_h \tag{14}$$

where $\mathbf{D}_h$ is the methane hydrate constitutive matrix.

It is assumed that the material damage and the subsequent changes in L can be related to the variation in the energy (per unit of volume) stored in the hydrates [30]. This energy can be defined as the elastic secant energy that would be recovered upon unloading; which, e.g., for triaxial conditions, can be written as [30]:

$$u_h = \frac{1}{2}\left(p_h\varepsilon_h^v + q_h\varepsilon_h^q\right) \tag{15}$$

The hydrate damage locus is defined by a threshold value 'r_0' of the secant elastic energy that can be represented by an ellipse in the 'p_h-q_h' space. The hydrate stiffness remains constant when the stresses are inside that ellipse. Loading damage takes place when the changes in the stress state is such that the secant elastic energy reaches r_0. During damage, the associated variable L increases, inducing a reduction of the material stiffness. The damage evolution is determined by means of the function below [32]:

$$r_{(L)} = r_0 e^{r_1 L} = u_h \tag{16}$$

The damage rate is controlled by r_1. The consistency condition is adopted for defining the evolution law for L [32]. The following evolution law for the partition variable is adopted:

$$\chi = \chi_0 e^{-\frac{L}{2}} \tag{17}$$

where χ_0 is an initial reference value assumed for the partition variable.

3.3. Constitutive model for the sediment skeleton

The constitutive model for the soil skeleton is based on a modified HISS framework. The constitutive equation incorporates subloading concepts, as well as hardening and dilation enhancement mechanisms associated with the presence of hydrates in the sediments. The modified HISS model involves a single and continuous yield surface that can adopt different shapes depending on the selected parameters [34–36]. The HISS yield surface (F) is given by:

$$F = \frac{a}{M^2}q_{ss}^2 - 9\gamma\left[\left(p'_{ss}\right)^2 - \left(p'_{ss}\right)^n p_c^{2-n}\right] \tag{18}$$

where a and γ are model constants; n is the parameter related to the transition from compressive to dilative behavior; p'_{ss} and q_{ss} are the mean effective and deviatoric stresses, respectively, both associated with the sediment skeleton; M is the slope of critical line in the q_{ss}-p'_{ss} space; and p_c is the effective pre-consolidation pressure. Fig. 6 presents some examples of yield surface shapes that can be adopted with this models, and Table 1 lists the corresponding parameters. The ellipse associated with the Modified Cam-Clay (MCC) yield surface is a particular case of this model.

The mean effective stress (p'_{ss}) and the elastic volumetric strains are related through the stress-dependent elastic sediment bulk modulus K'_{ss}:

$$K'_{ss} = \frac{v}{\kappa}p'_{ss} \tag{19}$$

where v is the specific volume; and κ is the slope of the unloading/reloading curve in the void ratio (e) versus log(p'_{ss}) space. The sediment-skeleton shear modulus (G_{ss}) relates the deviatoric elastic strains with the deviatoric stresses.

An isotropic strain hardening behavior in terms of the plastic volumetric deformation (ε^{vp}) is adopted:

$$\frac{dp_c}{p_c} = \frac{v}{\lambda - \kappa}d\varepsilon^{vp} \tag{20}$$

where λ is the slope of the normal compression line in the e-log(p'_{ss}) plane. It has assumed that the yield surface F and the plastic potential G coincide (i.e., associated plasticity). A non-associated flow rule can be easily incorporated if necessary.

$$d\boldsymbol{\varepsilon}^p = \Lambda\frac{\partial G}{\partial \boldsymbol{\sigma}'_{ss}} = \Lambda\frac{\partial F}{\partial \boldsymbol{\sigma}'_{ss}} \tag{21}$$

where Λ is the plastic multiplier and $\boldsymbol{\sigma}'_{ss}$ is the effective Cauchy's stress tensor.

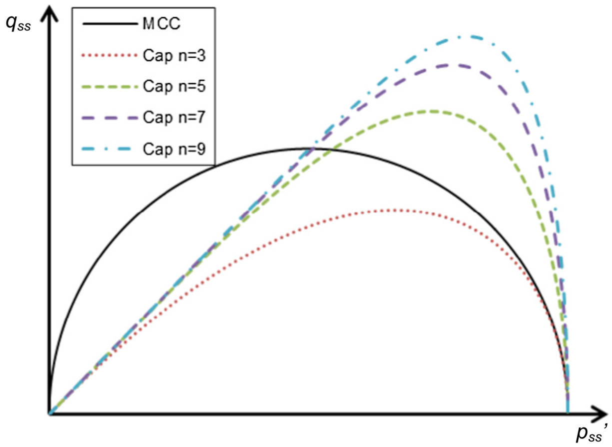

Fig. 6. Examples of yield surfaces shapes that can be adopted with the HIIS model.

Table 1
Parameters that control the shape of the yield surface in the HISS model.

Parameter	Modified Cam-Clay model (MCC)	Cap models
a	3	3
n	1	3, 5, 7, 9
γ	−1/9	1/9

The isotropic expansion of the yield surface is controlled by the hardening parameter 'p_d'. Based on [14], the influence of hydrates in this law is considered as:

$$p_d = \alpha(\chi C_h)^{\beta} \tag{22}$$

where α and β are constants that describe the degree of hydrate contribution to the hardening law. In all the analyses conducted in this work, a good agreement with the experimental data was obtained when $\beta = 1$, therefore this parameter could be excluded from the formulation, however it was kept to provide more flexibility to model in case is necessary. Also, previous works adopted a similar expression for p_d (e.g., [14]). Note that the presence of hydrate is also accounted when modeling the soil skeleton because of the profound impact of hydrates on sediment matrix behavior. Eq. (22) considers that once the hydrates fully dissociate, the behavior of the pure soil skeleton is recovered. The partition parameter χ (Eq. (17)) accounts for the effect of hydrate degradation on the preconsolidation pressure and it also provides a link between the damage law for the hydrates and the critical state model for the solid skeleton. The yield function (YF) incorporating the strength enhancement associated with the presence of methane hydrate can be expressed as:

$$F_b = \frac{a}{M^2} q_{ss}^2 - 9\gamma\left[(p'_{ss})^2 - (p'_{ss})^n (p_c + p_d)^{2-n}\right] \tag{23}$$

where F_b corresponds to an external (limit) surface, called hereafter boundary yield surface. This surface coincide with F when the effect of hydrates on the sediment matrix vanishes because of hydrate dissociation or damage.

To account for inelastic deformations that may occur inside the bounding yield-surface sub-loading concepts are incorporated into the model formulation. This technique also smooths the transition between elastic and plastic states. Sub-loading concepts were used before with success to model the behavior of HBS [11,14,15]. The sub-loading yield surface and the yield surface F, are geometrically similar. The sub-loading surface passes through the present stress state and it evolves during yielding. More details about sub-loading concepts can be found elsewhere (e.g., [59,60]). The modified sub-loading yield surface (F_s) incorporating p_d can be written as:

$$F_s = \frac{a}{M^2} q_{ss}^2 - 9\gamma\left\{(p'_{ss})^2 - (p'_{ss})^n [R(p_c + p_d)]^{2-n}\right\} \tag{24}$$

where R is the sub-loading surface ratio. As suggested by Hashiguchi [59,60], it is assumed that $0 < R \leqslant 1$. The changes in R are defined through the following evolution law [14,15]:

$$dR = -\eta \ln R |d\varepsilon^p| \tag{25}$$

where $|d\varepsilon^p|$ is the norm of the incremental plastic strain vector and η is a sub-loading parameter that controls the plastic deformations inside F_b. The term between brackets in Eq. (24) is called effective hardening parameter (i.e., $H = R(p_c + p_d)$). The three yield surfaces considered in this model are presented schematically in Fig. 7.

The consistency condition is enforced to ensure that the stress state remains on the (sub-loading) yield surface during yielding:

$$dF_s = \frac{\partial F_s}{\partial \boldsymbol{\sigma}'_{ss}} d\boldsymbol{\sigma}'_{ss} + \frac{\partial F_s}{\partial p_c} dp_c + \frac{\partial F_s}{\partial p_d} dp_d + \frac{\partial F_s}{\partial R} dR \tag{26}$$

After substituting the flow rule (21) into the consistency condition (26), the plastic multiplier can be obtained as:

$$\Lambda = \frac{\left(\frac{\partial F_s}{\partial \boldsymbol{\sigma}'_{ss}}\right)^T d\boldsymbol{\sigma}'_{ss} + \frac{\partial F_s}{\partial p_d} \alpha\beta\chi(C_h)^{\beta-1} dC_h}{\frac{\partial F_s}{\partial p_c}\left(\frac{v}{\lambda - k}\right) p_c \frac{\partial F_s}{\partial p'_{ss}} + \frac{\partial F_s}{\partial R}(-\eta)\ln R\left|\frac{\partial F_s}{\partial \boldsymbol{\sigma}'_{ss}}\right|} \tag{27}$$

The constitutive relationship for the sediment skeleton is obtained following the procedure suggested in [32]:

$$d\boldsymbol{\sigma}'_{ss} = \mathbf{D}_{ss} d\boldsymbol{\varepsilon} + \mathbf{d}_{C_h} dC_h \tag{28}$$

where

$$\mathbf{D}_{ss} = \left[\mathbf{D}^e_{ss} - \frac{\mathbf{D}^e_{ss} \frac{\partial F_s}{\partial \boldsymbol{\sigma}'_{ss}} \left(\frac{\partial F_s}{\partial \boldsymbol{\sigma}'_{ss}}\right)^T \mathbf{D}^e_{ss}}{\left(\frac{\partial F_s}{\partial \boldsymbol{\sigma}'_{ss}}\right)^T \mathbf{D}^e \frac{\partial F_s}{\partial \boldsymbol{\sigma}'_{ss}} + \frac{\partial F_s}{\partial p_c}\left(\frac{v}{\lambda - k}\right) p_c \frac{\partial F_s}{\partial p'_{ss}} + \frac{\partial F_s}{\partial R}(-\eta)\ln R\left|\frac{\partial F_s}{\partial \boldsymbol{\sigma}'_{ss}}\right|}\right] \tag{29}$$

$$\mathbf{d}_{C_h} = \left[\mathbf{D}^e_{ss} \frac{\frac{\partial F_s}{\partial p_d} \alpha\beta\chi(C_h)^{\beta-1} \frac{\partial F_s}{\partial \boldsymbol{\sigma}'_{ss}}}{\frac{\partial F_s}{\partial p_c}\left(\frac{v}{\lambda - \mathrm{k}}\right) p_c \frac{\partial F_s}{\partial p'_{ss}} + \frac{\partial F_s}{\partial R}(-\eta)\ln R\left|\frac{\partial F_s}{\partial \boldsymbol{\sigma}'_{ss}}\right|}\right] \tag{30}$$

where $\mathbf{D}^e_{ss}$ is the sediment skeleton elastic constitutive matrix, with a structure similar to Eq. (13) but K'_{ss} (i.e., Eq. (19)) and G_{ss} are used instead of K_{h0} and G_{h0}, respectively. Eq. (28) shows the effect of hydrates on effective stress; which in turns affects the mechanical behavior of HBS. This equation also shows that the effect of hydrates vanishes once they dissociate and the true response of the sediment matrix is recovered.

3.4. Final stress-strain relationships

To obtain the expressions relating the external effective stress $\boldsymbol{\sigma}'$ with the two stress components, the principle of virtual work is advocated, which for triaxial conditions can be written as [32]:

$$p' d\varepsilon^v + q d\varepsilon^q = p'_{ss} d\varepsilon^v + q_{ss} d\varepsilon^q + p_h C_h d\varepsilon^v_h + q_h C_h d\varepsilon^q_h \tag{31}$$

The following equation is obtained after replacing Eqs. (9) and (10) into Eq. (31):

$$p' d\varepsilon^v + q d\varepsilon^q = p'_{ss} d\varepsilon^v + q_{ss} d\varepsilon^q + p_h C_h \frac{\chi}{1 + C_h\chi} d\varepsilon^v + q_h C_h \times \frac{\chi}{1 + C_h\chi} d\varepsilon^q \tag{32}$$

Considering that the equation above is valid for any external strain:

$$p' = p'_{ss} + \frac{C_h\chi}{1 + C_h\chi} p_h \tag{33}$$

$$q = q_{ss} + \frac{C_h\chi}{1 + C_h\chi} q_h \tag{34}$$

For a given C_h the redistribution of external stress between hydrates and soil skeleton is given by χ. When χ decreases (i.e., when degradation is taking place), the mechanical contribution associated with the hydrates is progressively transferred to the sediment matrix. A similar phenomenon takes place during dissociation, and once the hydrates fully dissociate, the external stresses are equal to the soil skeleton ones (i.e., as expected, there is no contribution from the hydrates).

Considering Eqs. (33) and (34), the external (global) effective stress can be expressed as follows.

$$d\boldsymbol{\sigma}' = d\boldsymbol{\sigma}'_{ss} + \frac{C_h\chi}{1 + C_h\chi} d\boldsymbol{\sigma}_h \tag{35}$$

Finally, $d\boldsymbol{\sigma}'$ becomes:

$$d\boldsymbol{\sigma}' = \left[\mathbf{D}_{ss} + \left(\frac{\chi}{1 + C_h\chi}\right)^2 \mathbf{D}_h\right] d\boldsymbol{\varepsilon} + \left[\mathbf{d}_{C_h} + \boldsymbol{\sigma}_h\left(\frac{\chi}{1 + C_h\chi} - C_h\left(\frac{\chi}{1 + C_h\chi}\right)^2\right)\right] dC_h \tag{36}$$

The constitutive equations presented above provide the relationships between the external stresses in terms of hydrate and soil matrix stresses. Eq. (36) in particular expresses the changes in external effective stresses, when changes in total strains and

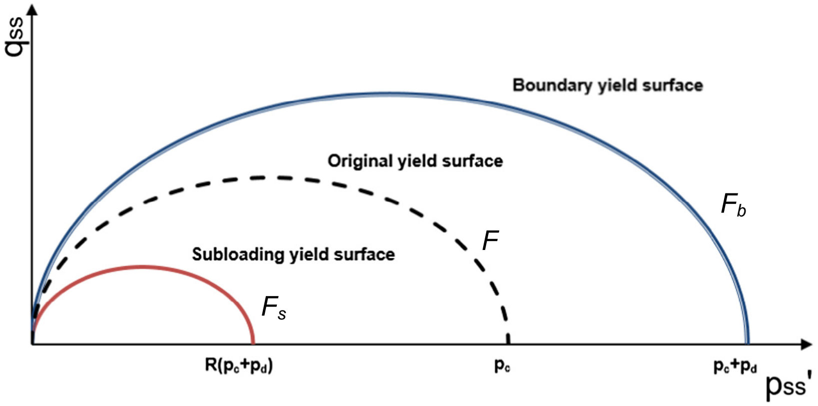

Fig. 7. Yield surfaces considered in the proposed model.

hydrate concentration take place. Note that C_h is acting as a 'pseudo-strain' (i.e., Eq. (36)), in the sense that changes in hydrate concentration also induce changes in effective stress.

4. Model application

The performance of the model presented in Section 3 was compared against available experimental data (most of them published recently) involving a variety of conditions, from tests at constant S_h, to experiments involving hydrate dissociation at constant stresses.

The hydrates parameters K_h and G_h can be considered material constants, therefore they were not changed in the analysis considered. They were from Miranda and Matsuoka [48]. As for the model related to the sediment skeleton, an ellipse (as in the MCC model) was adopted initially in all the cases. However, when the response based on the MCCM yield surface was not satisfactory, its shape was slightly modified to improve the model performance. This happened in the analyses corresponding to Cases 4.2 and 4.3 below, in all the other analyses the MCCM yield surface was adopted. More details about the determination of the model parameters are provided below in each one of the analyzed cases. It is also worth mentioning that the main aim of the modeling was not to exactly reproduce the experimental behavior, but to check whether or not the suggested approach was able to capture the main features of HBS behavior observed in these experiments.

The equations presented in Section 3 can be integrated numerically as suggested in Pinyol Puigmartí et al. [32]. The stress integration method proposed by Sloan [61] was adapted for the specific characteristics of this model [62]. All the analyses presented in this paper correspond to the 'point integration level' type. For the modeling of the tests loaded at constant hydrate concentration (i.e., cases below in Sections 4.1–4.3 and 4.5), dC_h was kept constant, changes in $d\varepsilon$ were introduced by steps and $d\boldsymbol{\sigma}'$ was updated correspondingly (see Eq. (36)). While for those cases in which hydrate dissociation was induced at constant effective stress (i.e., cases below in Sections 4.4 and 4.6), $d\boldsymbol{\sigma}'$ was hold constant, dC_h was changed by steps and Eq. (36) was solved in terms of $d\varepsilon$. All the experiments analyzed in this paper were conducted under drained conditions, this assumption was considered in the corresponding modeling.

4.1. Effect of hydrate saturation on HBS behavior

Hyodo et al. [39] reported triaxial compression tests on synthetic HBS samples conducted at four constant hydrate saturations (i.e., $S_h = 0$; 24.2; 35.1; and 53.1%). All the samples were prepared at a similar porosity (i.e., $\phi \sim 40\%$). The effective confining pressure for all the tests was 5 MPa. The samples were isotopically consolidated first and then subjected to shearing. The main test conditions related to this experimental study are listed in Table 2.

The model parameters were determined using back-analysis based on two tests, the one involving sediments without hydrates (i.e., $S_h = 0$) and the test related to the highest hydrate saturation (i.e., $S_h \sim 53.1\%$). Then, this model (without modifying the parameters adopted before) was used to predict the behavior of the samples with $S_h \sim 24.2\%$ and $S_h \sim 35.1\%$. Table 3 lists the parameters adopted in the numerical simulations. Fig. 8a and b shows the comparisons between experimental and model results for the different hydrate saturations in terms of deviatoric stress and volumetric strains versus axial strains. The specimen corresponding to hydrate saturation equal to 53.1% presents a (slight) stress-softening (post-peak) behavior and a dilatant response; while all the other samples exhibits a predominant compression behavior. The relatively high confining pressure at which these tests were performed (i.e., $\sigma'_c = 5$ MPa) could be one reason for the predominant hardening behavior with positive volumetric strains observed in the experiments. In all the tests the initial stiffness and shear strength increase with S_h. The model was able to match very satisfactorily the stress-strain curves for all the experiments under study, i.e., the ones used for calibration and also the others two prediction tests. The agreements between tests and models results in terms of volumetric behavior were also excellent (Fig. 8b).

4.2. Effect of hydrate morphology on HBS behavior

Triaxial compression tests based on synthetic methane hydrate samples were performed by Masui et al. [29]. Some specimens were prepared using the ice-seed method that generally produces gas hydrates with dominant pore-filling pore-habit [29]. For other samples, the partial water saturation method was adopted, which generally leads to HBS where the cementing morphology type is dominant [29]. Toyoura sand was adopted for all the tests. These specimens were tested in a triaxial device capable of reproducing fluid pressures equivalent to conditions of around 800 m under

Table 2
Test conditions for triaxial compression tests studied in Section 4.1.

Effective confining pressure (MPa)	Porosity (%)	S_h (%)
5	39.4	0
	39.6	24.2
	39.2	35.1
	40.1	53.1

Table 3
Soil parameters adopted in the modeling of HBS in Section 4.1.

Properties	Test $S_h = 0$	Test $S_h = 24.2\%$	Test $S_h = 35.1\%$	Test $S_h = 53.1\%$
M	1.30	1.30	1.30	1.30
λ	0.16	0.16	0.16	0.16
κ	0.004	0.004	0.004	0.004
p_c (MPa)	10.0	10.0	10.0	10.0
a	3	3	3	3
n	1	1	1	1
γ	−1/9	−1/9	−1/9	−1/9
C_h (initial)	0	0.096	0.138	0.213
α	–	32	32	32
β	–	1.0	1.0	1.0
r_1	–	4.1	4.1	4.1
r_0	–	1e−5	1e−5	1e−5
η	42	42	42	42
χ_0	–	1	1	1
K_h (MPa)	–	9600	9600	9600
G_h (MPa)	–	4300	4300	4300

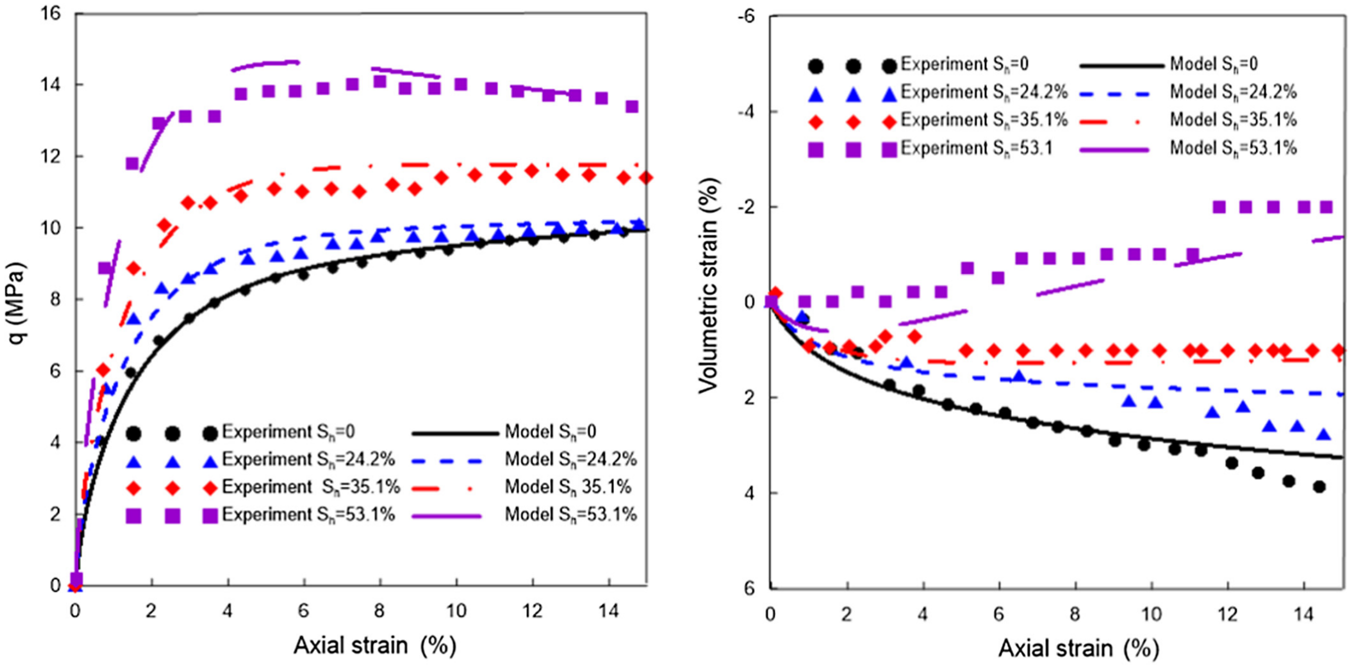

(a)

(b)

Fig. 8. Comparisons between model and experimental results for synthetic samples of HBS prepared at different hydrate saturations: (a) stress-strain behavior and (b) volumetric response. Experimental data adapted from [39].

sea level. The tests were conducted at a $\sigma'_c = 1.0$ MPa. No hydrate dissociation was induced during the experiments.

The three experiments presented in Fig. 2b carried out by Masui et al. [29] were selected to study the capability of the model to reproduce the effect of hydrate morphology on the mechanical behavior of HBS. The main parameters adopted for the numerical analysis are listed in Table 4. Masui et al. [29] reported porosity values between 37.7% and 42.4%. The hydrate saturation was very similar in both tests (i.e., $S_h \sim 0.41$).

Fig. 9 shows the comparisons between experimental results and model outputs in terms of stress-strain and volumetric behaviors. The model was able to capture very satisfactorily the different features of HBS behavior (i.e., increase of stiffness, strength and dilation in the samples with hydrates) observed in these tests involving different hydrate morphologies and pure sediment. The model was able to satisfactorily capture the more marked mechanical effect that the cementing form has on HBS behavior when compared against the pore-filling morphology type. One issue to

Table 4
Soil parameters adopted in the modeling of Cases in Section 4.2.

Properties	Pure sand	Pore-filling	Cementing
M	1.17	1.17	1.17
λ	0.18	0.18	0.18
κ	0.006	0.006	0.006
p_c (MPa)	12	12	12
a	3	3	3
n	1.02	1.02	1.02
γ	−1/9	−1/9	−1/9
C_h (initial)	0	0.16	0.16
α	–	35	70
β	–	1.0	1.0
r_1	–	1.1	1.05
r_0	–	7e−5	1e−4
η	15	15	15
χ_0	0	1.0	1.5
K_h (MPa)	–	9600	9600
G_h (MPa)	–	4300	4300

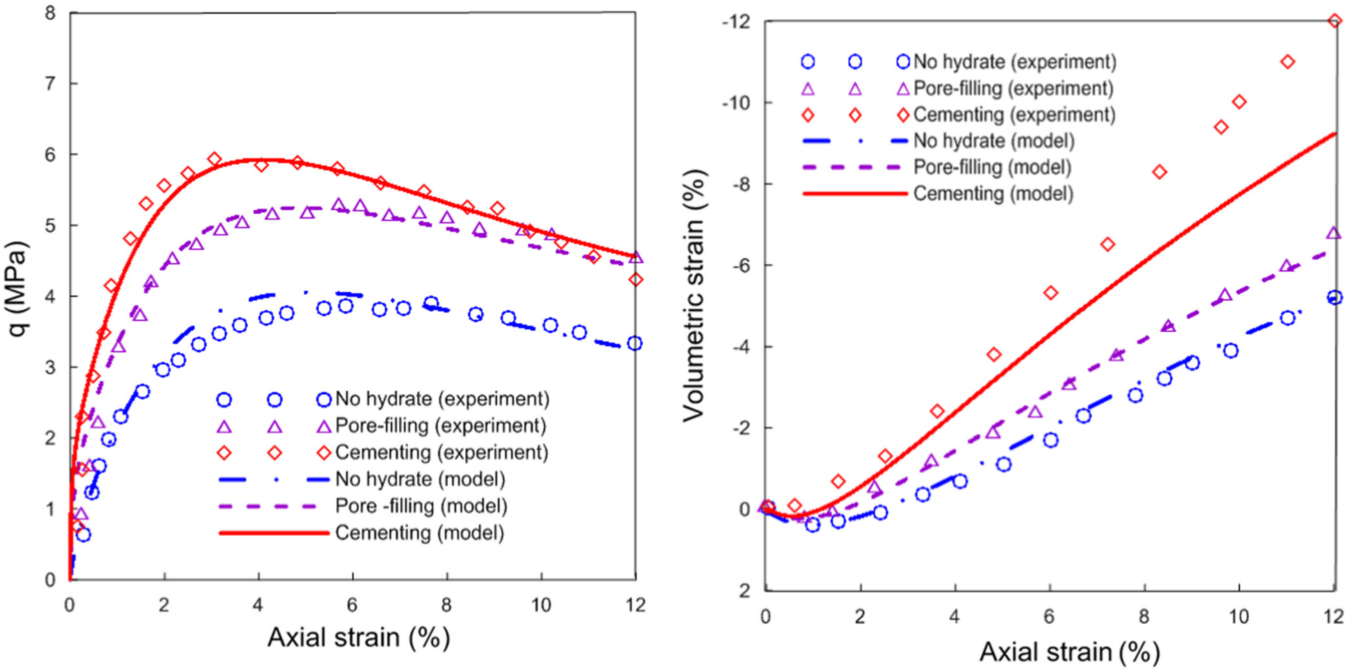

(a) (b)

Fig. 9. Comparisons between model and experimental results for synthetic Toyoura sand samples with different hydrates pore habits: (a) stress strain behavior and (b) volumetric response. Experimental data adapted from [29].

note is that the model under-estimate the sediment dilatancy and softening for the cementing case. Note that the same HISS model parameters were adopted for the sediment in the three cases since they do not depend on the hydrates pore-habit. As discussed before, it was assumed that the initial strain-partition parameter χ_0 (i.e., Eq. (17)) depends on hydrate morphology. The value of the cementing sample was adopted higher (i.e., $\chi_0 = 1.5$) than the pore-filling one (i.e., $\chi_0 = 1.0$).

4.3. Modeling the behavior of natural HBS samples

Synthetic methane hydrate specimens were modeled in the two previous Sections, in this one, experiments involving natural hydrate samples conducted by Yoneda et al. [63] are studied. Core samples were retrieved from the Eastern Nankai Trough by means of the pressure core analysis and transfer system. The natural sediments were maintained very close to the in-situ condition [56]. Table 5 lists the main soil properties and other information associated with these experiments. Specimens identified as core#7 and core#9, with $S_h \sim 38\%$ and $S_h \sim 79\%$, respectively, were tested under triaxial drained conditions. As explained in Yoneda et al. [63], the manipulation of core#9 and core#7 induced changes in the material. Core#7 was treated using liquid nitrogen (LN_2) core method, while core#9 was treated using CH_4 purge LN_2 core method. In these two methods, the specimens were exposed to the atmospheric pressure, which might induce hydrate dissociation. Yoneda et al. [63] suggested that the plausible in-situ hydrate saturation for core#7 could be between 65% and 90%, but because of the sample handling, the hydrate saturation decreased up to ~38% (i.e., at test condition). Furthermore, some damage of the core was observed in the CT images which means that the soil structure was affected by the handling method. As for core#9, the in-situ hydrate saturation was between 70% and 95%. It was also estimated that the hydrate saturation at test condition was around 79%. Furthermore, no damage was observed in this specimen which implies that when core#9 was tested at conditions similar to the field ones. Based on the comments above these two cores correspond to different materials and therefore slightly different parameters were assumed in the simulation of these two cases. However, the same critical state parameters were assumed for both cases because they are not related to the hydrate morphology. Table 6 lists the adopted parameters.

Fig. 10 presents the experimental and numerical results for the stress-strain behavior and volumetric response of the natural HBS core samples discussed above. Core#9 exhibits a very noticeable peak strength, with a significant enhancement in stiffness and dilatancy, which can be associated with the higher hydrate saturation of this sample respect to core#7. As shown in Fig. 10, the model provides enough flexibility to satisfactorily reproduce the mechanical behavior of two natural samples from Nankai Trough. The performance of the model is very satisfactory but for some slight deviations in terms of volumetric strain.

4.4. Effect of hydrate dissociation on HBS behavior under triaxial conditions

The tests conducted by Hyodo et al. [37] were selected to study the effect of hydrate dissociation under triaxial conditions. The

Table 5
In situ conditions, soil index properties, and testing conditions for tests presented in Section 4.3.

Test name	Host type	Overburden (m)	σ'_3 (MPa)	Water content (%)	ϕ (%)	S_h (%)
#7	Silty sand	279.3	1.5	26.4	44.1	38
#9	Silty sand	294.2	1.6	22.7	39.4	79

main information about the samples and tests details were introduced in Section 2.2. Table 7 lists the main tests conditions related to these experiments.

These tests provide very useful information about the effect of hydrate dissociation at two stages of shearing. When the dissociation was induced at $\varepsilon_a = 1\%$, the stress conditions were quite far from the failure of the dissociated sediment (i.e., the deviatoric stress of this sample at $\varepsilon_a = 1\%$ was 8.4 MPa, while the strength at failure of the already dissociated sample was around 10 MPa, Fig. 3a). However, when the hydrate dissociation started at $\varepsilon_a = 5\%$ the deviatoric stress (i.e., $q \approx 12$ MPa) was higher than the strength of the dissociated sediment and it was difficult to maintain the constant stress condition during dissociation. The sample failed and the deviatoric stress reduced tending to the strength of the dissociated sample (i.e., $q \approx 10$ MPa). These were quite complex experiments that have been simulated following, as close as possible, the reported test protocols [37].

The modeling of these experiments was approached as follows: (i) first the test related to the already dissociated sediment was simulated (using typical reported parameters for this type of material, i.e., sand); then, (ii) the test related to the dissociation at $\varepsilon_a = 1\%$ was studied (and used to adjust the model parameters for the HBS case); and finally, (iii) the test involving hydrate dissociation at an initial $\varepsilon_a = 5\%$ was simulated to validate the proposed model under these particular conditions. Table 8 lists the main parameters selected for the modeling.

Table 6
Soil parameters adopted in the modeling of HBS specimens presented in Section 4.3.

Properties	Core 7	Core 9
M	1.26	1.26
λ	0.16	0.16
κ	0.014	0.014
p_c (MPa)	12	12
a	3	3
n	0.98	0.98
γ	−0.14	−0.14
C_h (initial)	0.1675	0.311
α	6	21
β	1	1
r_1	1.1	1.3
r_0	1e−5	1.25e−4
η	3	48
χ_0	1	1
K_h (MPa)	9600	9600
G_h (MPa)	4300	4300

Table 8
Parameters adopted in the modeling of HBS specimens. Section 4.4.

Properties	Shear after dissociation	Dissociation induced at $\varepsilon_a = 1\%$	Dissociation induced at $\varepsilon_a = 5\%$
M	1.17	1.17	1.17
λ	0.12	0.12	0.12
κ	0.002	0.002	0.002
p_c (MPa)	11.5	11.5	11.5
a	3	3	3
n	1	1	1
γ	−1/9	−1/9	−1/9
C_h (initial)	0	0.195	0.195
α	–	16	16
β	–	1.0	1.0
r_1	–	2.9	2.9
r_0	–	1e−5	1e−5
η	–	35	35
χ_0	–	3	3
K_h (MPa)	9600	9600	9600
G_h (MPa)	4300	4300	4300

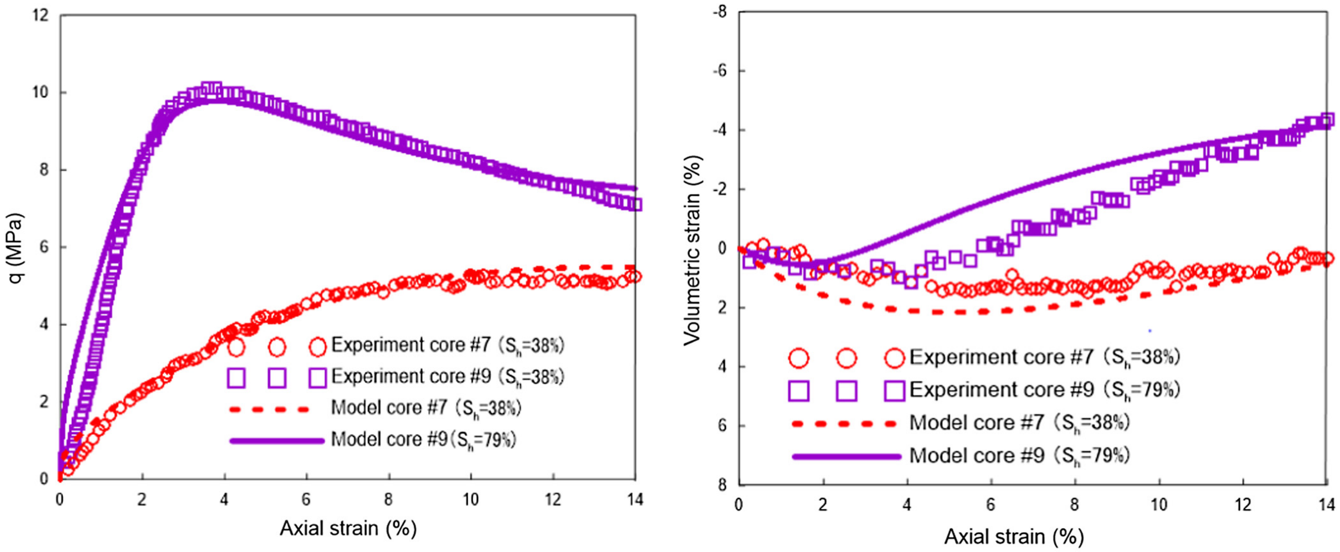

(a) (b)

Fig. 10. Comparisons between model and experimental results for triaxial tests on natural samples: (a) stress strain behavior and (b) volumetric response. Experimental data adapted from [63].

Table 7
Test conditions of methane hydrate dissociation tests. Section 4.4.

Consolidation condition	σ'_c (MPa)	S_h (%)	Porosity (%)	Test N°	Remarks
Isotropic	5	48.7	40.4	1	Dissociation → Shear
Isotropic	5	47.4	39.9	2	Shear 1% → Dissociation → Shear
Isotropic	5	47.9	39.8	3	Shear 5% → Dissociation → Shear

Fig. 11 presents the comparisons between experiment and model results for the three cases discussed above. As for the already dissociated sample (Fig. 11a), quite good agreements were obtained in terms of deviatoric stress and volumetric behavior. In particular, the model manages to replicate well the maximum stress, but slightly under-predicts the maximum volumetric strain. Fig. 11b presents the experimental and numerical results related to the sample at which dissociation was induced at $\varepsilon_a = 1\%$. In addition to the external deviatoric stresses (i.e., the one to be compared against the experimental observations), the mechanical contributions of the hydrate and sediment skeleton are computed by the model and included in this figure as well.

Initially, both hydrate and sediment contributed progressively to the mechanical stability of the specimen. Afterwards, during hydrate dissociation, the mechanical contribution arising from the hydrate was progressively decreasing and transferred to the soil skeleton, leading to an increase in the sediment stress during this step at constant global stress. The external stress is solely supported by the soil skeleton at the end of the dissociation process. Shearing continued after full dissociation and the deviatoric stress

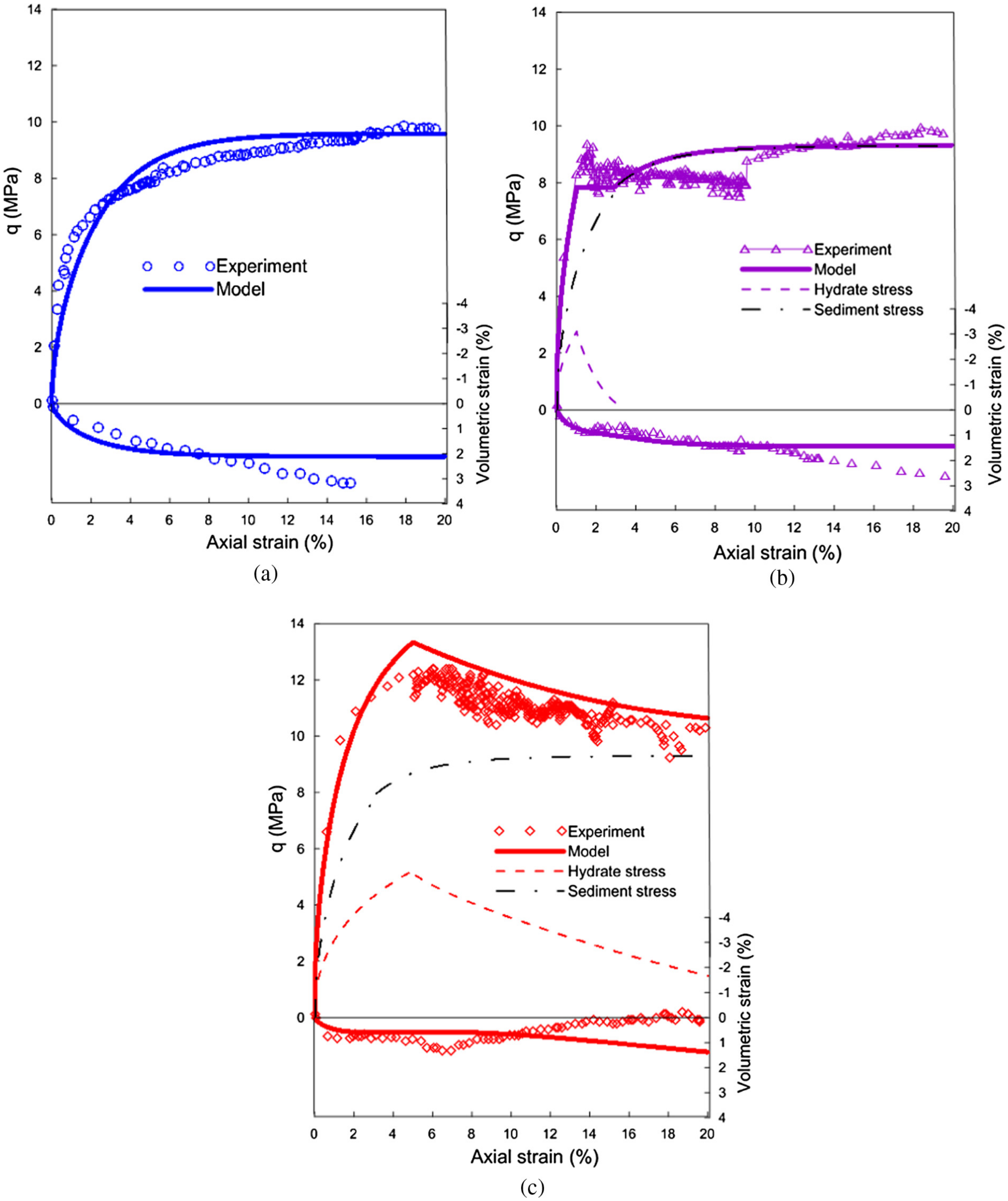

(a)

(b)

(c)

Fig. 11. Experimental and modeling results for drained triaxial tests: (a) already dissociated sediment, (b) dissociation induced at $\varepsilon_a = 1\%$; and (c) dissociation induced at $\varepsilon_a = 5\%$. Experimental data adapted from [37].

increased until reaching the strength of the already dissociated sediment.

The model captures very satisfactorily the main trends observed in these experiments, particularly: the degradation in stiffness during the initial loading stage, the (average) deviatoric stress during dissociation, and the maximum final deviatoric stress after dissociation. However, the experimental deviatoric stress at $\varepsilon_a = 1\%$ is slightly higher than the one computed by the model, and the axial strains observed during dissociation are larger than the simulated ones. Note that in any case, the volumetric deformations during dissociation are well reproduced by the model. The model slightly under-predicts the ε_v at advanced stages of the experiment (i.e., $\varepsilon_a > 12\%$). At that final stages of shearing, the three yield surfaces considered in this model coincided in one, and the stress state is on the summit of that ellipse. Therefore, according to the model, there are not changes in plastic volumetric strains (i.e., $d\varepsilon^{vp} = 0$) and ε^{vp} remains fairly constant. In this way the model simulates the material failure (i.e., continuous deformations at constant deviatoric stress). More details about how the different mechanisms adopted in this model work are presented in the following case.

Once the model parameters were calibrated using the two previous cases, the ability of the constitutive equation to predict the HBS behavior under dissociation was checked against the third test. Fig. 11c presents the comparisons between the experimental results and the model predictions for the case in which the hydrate was dissociated at $\varepsilon_a = 5\%$. The model results are also very satisfactory in this case, the main tendencies observed in this experiment are well captured by the model. However, the peak deviatoric stress is slightly over-predicted by the model. There are also some differences between the model predictions and the reported experimental data in terms of volumetric behavior. Surprisingly, it was observed that there was not volume change at the end of this test, because an apparent dilation during dissociation compensate the initial positive volumetric strains. This final dilation in the experimental result seems strange, the tendency during dissociation at high stresses under drained conditions should be to contract, because the sediment structure tend to a more compact state as the hydrates disappear. The positive ε^v predicted by the model during dissociation are related to the volumetric compression plastic strains induced by the collapse of the sediment structure during hydrate dissociation (as shown in Fig. 3b, and illustrated in Fig. 4b). This structure-collapse behavior is explained in more detail in Section 4.6.

Hyodo et al. [37] experienced some difficulties to maintain the deviatoric stress constant during dissociation in this test. Because of the progressive degradation of the HBS structure during hydrate dissociation, it was impossible to hold the (high) deviatoric stress applied just before dissociation (i.e., at $\varepsilon_a = 5\%$) [37]. The mechanical contribution from the hydrate (dash line) was gradually transferred to the sediment skeleton during dissociation, and the global deviatoric stress decreased progressively until reaching the maximum strength associated with the already dissociated sediment. At the end of shearing phase, the model predicts that hydrates still contribute to the mechanical behavior of the sample, this result is supported with the reported experimental data indicating that not all the hydrates dissociated at the final axial strain (i.e., $\varepsilon_a = 20\%$).

Fig. 12 shows additional information about this modeling. Fig. 12a presents the q-ε_a plot extended until full dissociation. As discussed before, during dissociation the bearing capacity of the hydrates decreased and the stress were gradually transferred to the sediment. The model predicts that at advanced stages of shearing and hydrate dissociation all the external stresses are supported by the sediment skeleton only. The effective hardening parameter ($H = R(p_c + p_d)$) always increased (Fig. 12b). This implies that F_s kept

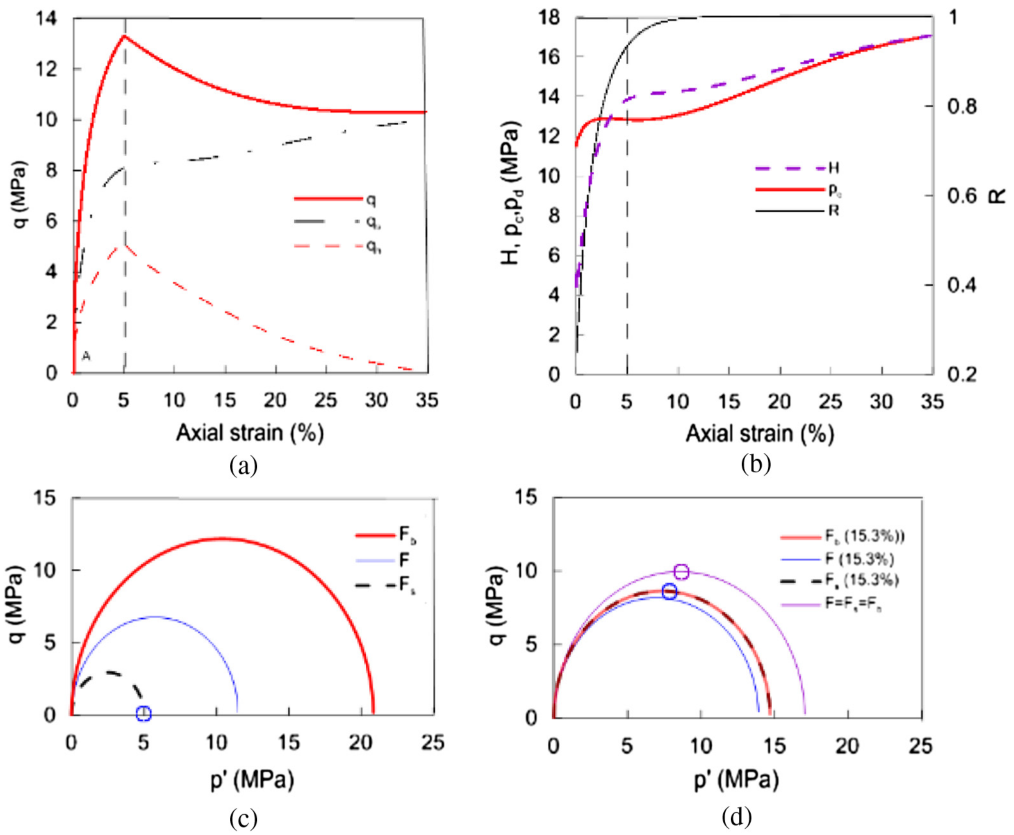

(a) (b)

(c) (d)

Fig. 12. Additional modeling information for the test in which dissociation was induced at $\varepsilon_a = 5\%$: (a) extended stress-strain behavior; (b) hardening variables, (c) yield surfaces at the beginning of the experiment; and (d) yield surfaces at an intermediate stage of shearing ($\varepsilon_a = 15.3\%$) and at the end of test.

expanding during the whole test. The variable R always increased during the simulation as well (Fig. 12b). The increase in H (i.e., hardening of the sediment skeleton) observed at advanced stages of the experiment was induced by the volumetric-collapse-compression strains discussed above; which compensated the decrease of p_d during hydrate dissociation. Fig. 12c presents the three initial yield surfaces (i.e., F, F_s, and F_b) considered in this model at the start of the test. Fig. 12d presents again these three yield surfaces at two different stages: (i) at $\varepsilon_a = 15.3\%$, i.e., when the sub-loading yield surface reached the boundary one (F is still inside $F_b = F_s$, because p_d did not vanish totally at this stage); and (ii) at the end of the test, when the three yield surfaces coincided in one.

The proposed model has not only reproduced and predicted satisfactorily the behavior observed in the experiments, but it has also provided an explanation to the main features and trends of HBS behavior observed during the tests. In the tests, the hydrate dissociation was induced by heating [37]. Thermal effects were not modeled in this analysis. This seems a reasonable assumption as the main focus here was on the influence of hydrates dissociation on material behavior. It also seems that temperature may have a small influence on the overall mechanical behavior of the specimen in this type of experiment. A more sophisticated analysis can certainly be done in the future incorporating thermal effects. The inclusion of temperature could also help to reproduce these experiments more closely.

4.5. Effect of coffining pressure and χ_0 on HBS response

Once the ability of the model to reproduce the main tendencies observed in the experiments was checked, it could be of interest to see how other factors (not modeled in the cases before) have an influence on the behavior of HBS. It can also be relevant to explore further about how the different parameters and inelastic mechanisms proposed in this model work to simulate the main features of HBS behavior.

The first analysis in this section is relate to the effect of confinement on HBS behavior. The study is based on the HBS specimen presented in Section 4.4. Tests at two additional cell pressures were simulated (i.e., $\sigma'_c = 1$ MPa and $\sigma'_c = 3$ MPa) and dissociation was not induced in this modeling (i.e., shearing at constant $S_h = 48\%$). Table 9 lists the adopted model parameters. Fig. 13a and b shows that the confinement plays a critical role in the behavior HBS, as σ'_c decreases the peak strength decreases, the dilatancy increases and also the softening is more marked.

Table 9
Parameters adopted in the modeling of HBS specimens in Section 4.5. Effect of confining pressure.

Properties	$\sigma'_3 = 1$ (MPa)	$\sigma'_3 = 3$ (MPa)	$\sigma'_3 = 5$ (MPa)
M	1.17	1.17	1.17
λ	0.12	0.12	0.12
κ	0.002	0.002	0.002
p_c (MPa)	11.5	11.5	11.5
a	3	3	3
n	1	1	1
γ	−1/9	−1/9	−1/9
C_h (initial)	0.195	0.195	0.195
α	16	16	16
β	1.0	1.0	1.0
r_1	2.9	2.9	2.9
r_0	1e−5	1e−5	1e−5
η	35	35	35
χ_0	3	3	3
K_h (MPa)	9600	9600	9600
G_h (MPa)	4300	4300	4300

The plots in Fig. 14 show more details about how the main variables of the model evolve for the test at $\sigma'_c = 1$ MPa. The hardening or softening behavior of the sediment is controlled by the effective hardening parameter H, which depends on R, p_c and p_d through $H = R(p_c + p_d)$. It is assumed that the plastic deformations of the soil skeleton take place from the beginning of yielding. This is in line with previous works in this area (e.g., [11,14,15]). Under this assumption, the model predicts plastic positive volumetric strains at the start of the test (i.e., between 'A' and 'B', Fig. 14a and b), because the stress state lies on the 'wet side' of F_s (Fig. 14c), therefore p_c increases. After point 'B', p_c decreases because the stress state is on the 'dry side' of F_s. The sub-loading parameter R increases during the whole test (as it depends on the module of the total plastic strain). The hardening enhancement provides by the hydrates (p_d) decreases through the tests due to progressive damage of the hydrates, up to reaching a fairly constant value. After the peak value 'C', the softening of the soil skeleton controls the global behavior of the HBS and the deviatoric stress tends to decrease substantially. The dilatant behavior of the skeleton also controls the global volumetric response of the HBS. Fig. 14c and d presents the yield surfaces associated with this model at different stages of the test.

Finally, a study related to the effect of the partition parameter χ_0 on the model response is conducted. This factor controls the amount of the applied stress that is supported by the hydrate. The analysis discussed before with $\sigma'_c = 1$ MPa and $\chi_0 = 3$ was adopted as the base case, and two additional analyses were performed with $\chi_0 = 2$ and $\chi_0 = 1$. The reduction of this factor is related to a decrease of the bearing contribution of the hydrate and also with a reduction of the peak deviatoric strength (Fig. 15a). The volumetric behavior of the HBS is also affected by this parameter (Fig. 15b), a reduction of χ_0 is accompanied by an increase in the dilatancy. The adopted parameters are listed in Table 10.

4.6. Effect of hydrate dissociation on HBS behavior under oedometric conditions

The last set of experimental data studied in this work corresponds to two natural specimens gathered by means of the Pressure Core Characterization Tools (PCCTs) [55,56]. The samples were loaded uniaxially with lateral confinement (i.e., oedometric conditions). General information about this research was presented in Section 2.2. The test presented in Fig. 3b) plus another one with a lower hydrate saturation are simulated in this section. The parameters reported [55] for the dissociated sediment (i.e., a silty sand) were adopted in the simulations. The selected parameters are listed in Table 11.

Tests and models outputs related to the specimen 'core-8P' (i.e., initial $S_h = 18\%$) are presented in Fig. 16a. The HBS specimen was subjected to a monotonic increase in the vertical stress up to $\sigma'_v = 6$ MPa, followed by an unloading up to $\sigma'_v = 3$ MPa. Hydrate dissociation was induced in this over-consolidated sample followed by cycles of loading (with a maximum $\sigma'_v = 9$ MPa) and unloading of the already dissociated sediment. The experimental and numerical results associated with specimen 'core-10P' (i.e., initial $S_h = 74\%$) are presented in Fig. 16b. In this case the effective vertical stress was increased until $\sigma'_v = 3$ MPa and hydrate dissociation was induced at this constant effective stress (under normally-consolidated conditions). Once the sample was fully dissociated, the vertical stress was increased until a maximum $\sigma'_v = 9$ MPa, followed by an unloading. Settlements were recorded in the both tests during all the loading stages.

The proposed framework was able to represent very satisfactorily the main tendencies observed in the experiments. The yield stress and unloading-reloading behavior are properly reproduced in both specimens. The model slightly over-predicts the initial

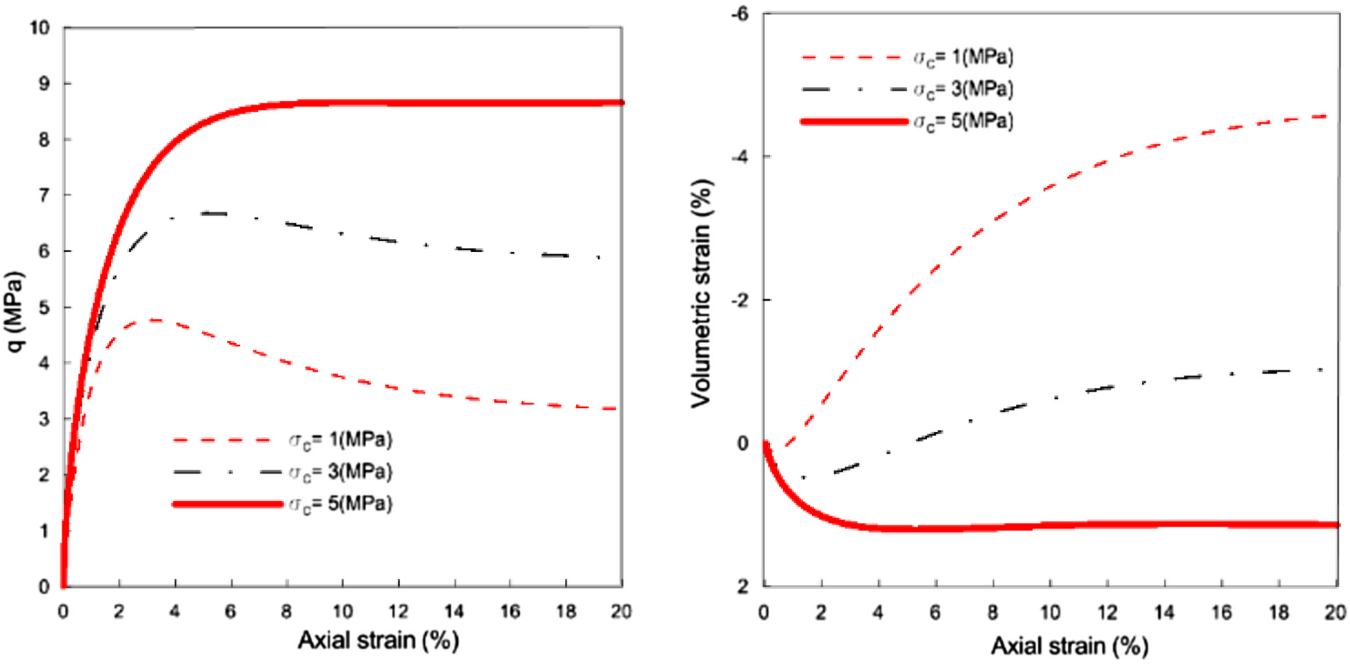

(a) (b)

Fig. 13. Effect of confinement on HBS response: (a) stress strain behavior and (b) volumetric response.

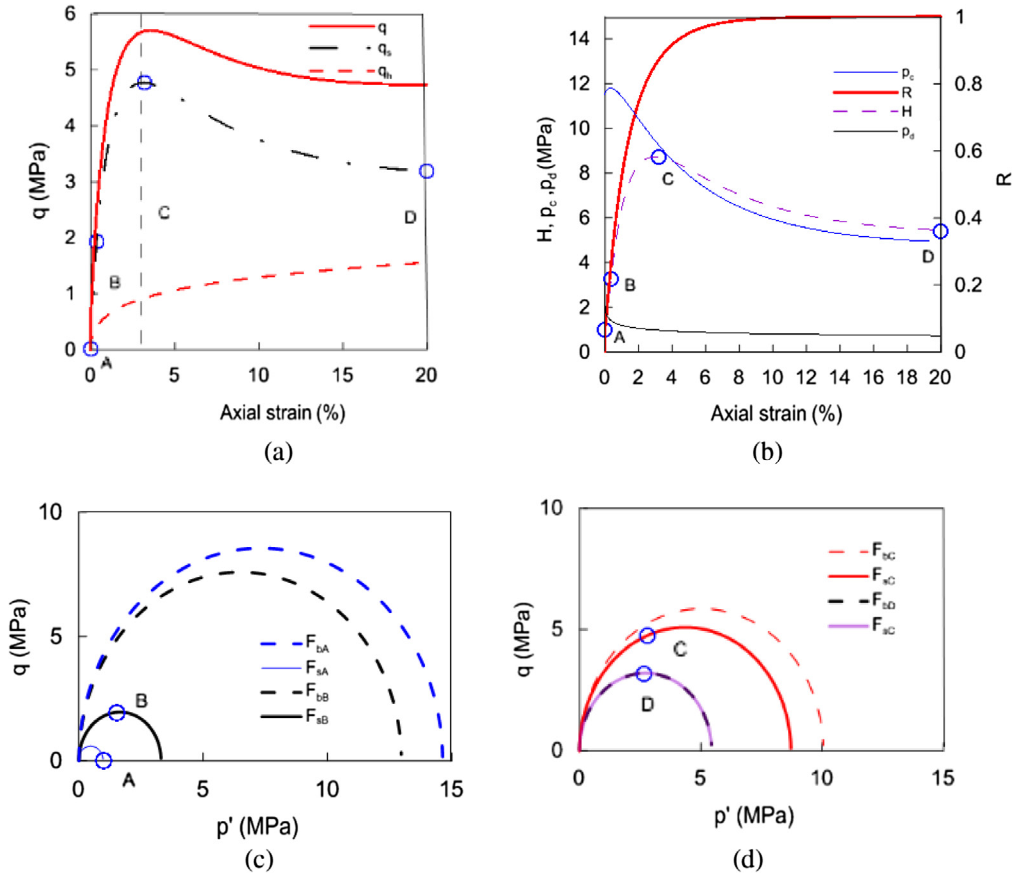

(a) (b)

(c) (d)

Fig. 14. Additional modeling information for the test in Fig. 13 at $\sigma'_c = 1$ MPa: (a) stress-strain behavior; (b) hardening variables; (c) yield surfaces at two initial stages of the experiment A&B; and (d) yield surfaces at two final stages of shearing C&D.

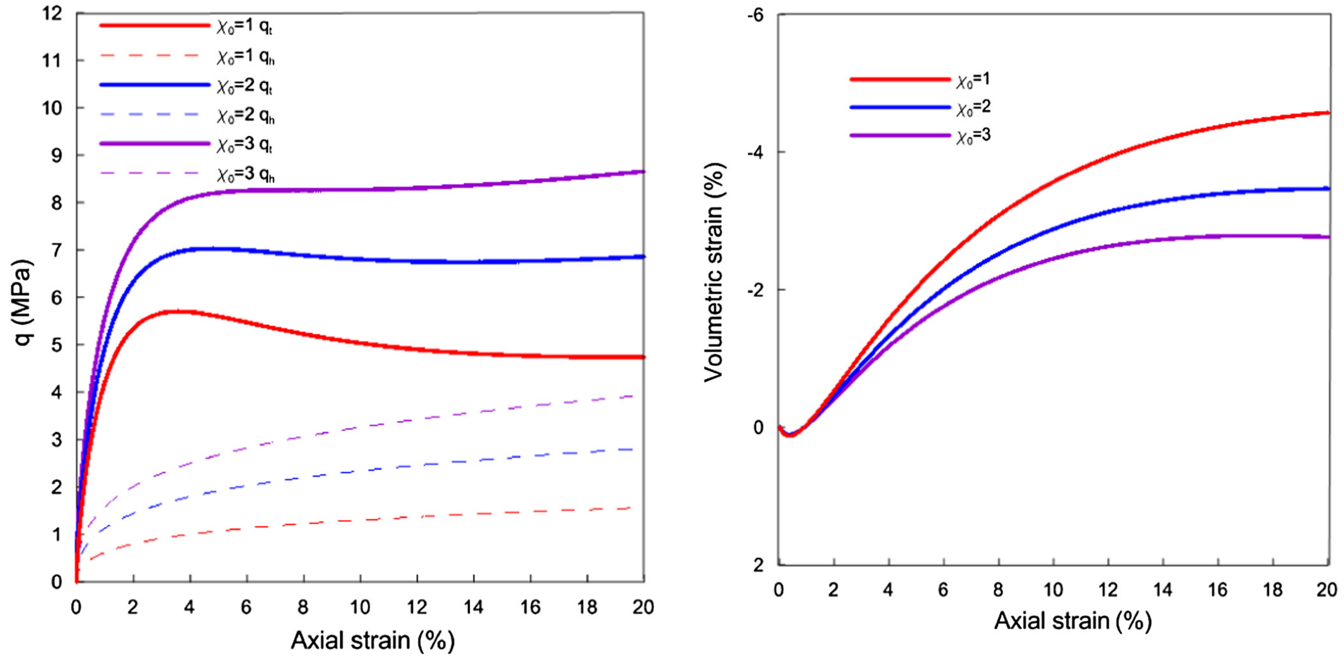

(a) (b)

Fig. 15. Effect of χ_0 on HBS response: (a) stress-strain behavior and (b) volumetric response.

Table 10
Parameters adopted in the modeling of HBS specimens in Section 4.5. Effect of parameters[a]: χ_0.

χ_0	r_0	r_1
1	$1e^{-5}$	2.9
2	$1e^{-5}$	2.9
3	$1e^{-5}$	2.9

[a] The parameters of the test in Table 9 with $\sigma'_3 = 1$ (MPa) was used as the base case for the parameter sensitivity study.

Table 11
Parameters adopted in the modeling of HBS specimens in Section 4.6.

Properties	Core 8P	Core 10P
M	1.07	1.07
λ	0.605	0.12
κ	0.065	0.04
p_c (MPa)	2.32	3.5
a	3	3
n	1	1
γ	−1/9	−1/9
C_h (initial)	0.102	0.3605
α	6	12.5
β	1.0	1.0
r_1	2.5	2.9
r_0	1e−6	2e−7
η	15	0.5
χ_0	1	3
K_h (MPa)	9600	9600
G_h (MPa)	4300	4300

stiffness of the core-10P. It is worth to highlight the model ability to reproduce the differences in volumetric strains observed during dissociation at constant stress in these two tests. The collapse compression behavior exhibited by core-8P was much less noticeable than the one observed in core-10P. This large volumetric strains can be associated with significant rearrangements of the HBS structure during hydrate dissociation. Some factors that can be considered to explain the differences between core-8p and core-10p in terms of the amount of the volumetric strain observed during dissociation are as follows: (i) difference in hydrate saturation between the two samples (i.e., core-8P $S_h = 18\% \ll$ core-10P $S_h = 74\%$); (ii) difference in the effective vertical stress at which hydrates dissociation was induced (i.e., core-8P $\sigma'_v = 3$ MPa $\ll$ core-10P $\sigma'_v = 8$ MPa), therefore the effect of confinement on the re-accommodation of the sediments particles is less significant for core-8p; (iii) dissociation in core-8P took place under over-consolidated conditions while in core-10p dissociation happened under normally-consolidated conditions; and (iv) core-8p was previously loaded up to a very high effective vertical stress (i.e., $\sigma'_v = 6$ MPa) that degraded the bonding effects of the hydrate and induced important changes in the sediment structure previous to dissociation.

Fig. 17a presents the evolution of σ'_v calculated by the model in the soil skeleton and hydrate, together with the global (or external) one for the case of core-8P. A significant portion of the stress increase is taken by the hydrate at the beginning of the experiment, i.e., path 'A-B'. Note that the hydrate saturation is very high in this case (i.e., $S_h = 74\%$) and therefore an important bearing contribution from the hydrate can be anticipated. Upon dissociation at constant effective stress, the load is gradually transferred from the hydrate to the sediment skeleton and significant plastic volumetric strains are computed by the model, i.e., path 'B-C'. After full dissociation, the stresses are supported by the soil skeleton only, and the subsequent loading ('C-D') and unloading ('D-E') steps are controlled by the properties of the already dissociated sediment. Fig. 17b shows that the hardening enhancement effect (controlled by p_d) reduces progressively during loading and it disappears during dissociation. The effective hardening parameter H increases during loading and remained unchanged upon unloading.

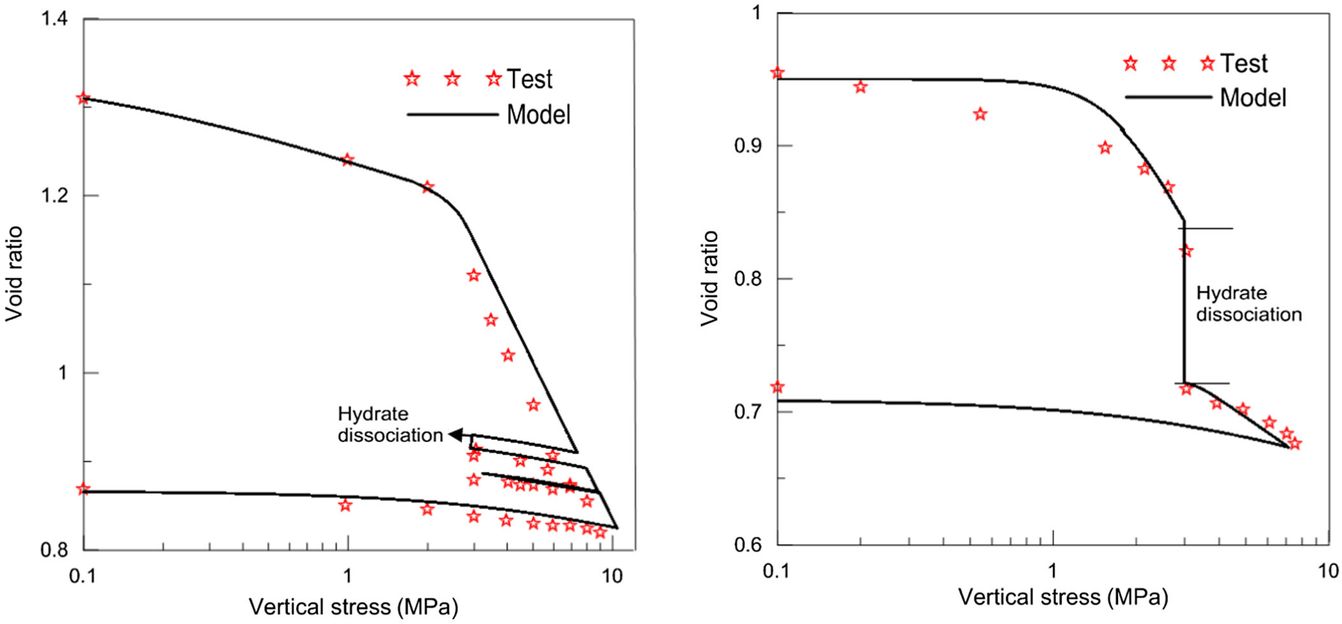

(a)

(b)

Fig. 16. Behavior during dissociation of natural HBS specimens under oedometric conditions: (a) core 8P and (b) core 10P. Experimental data adapted from [55].

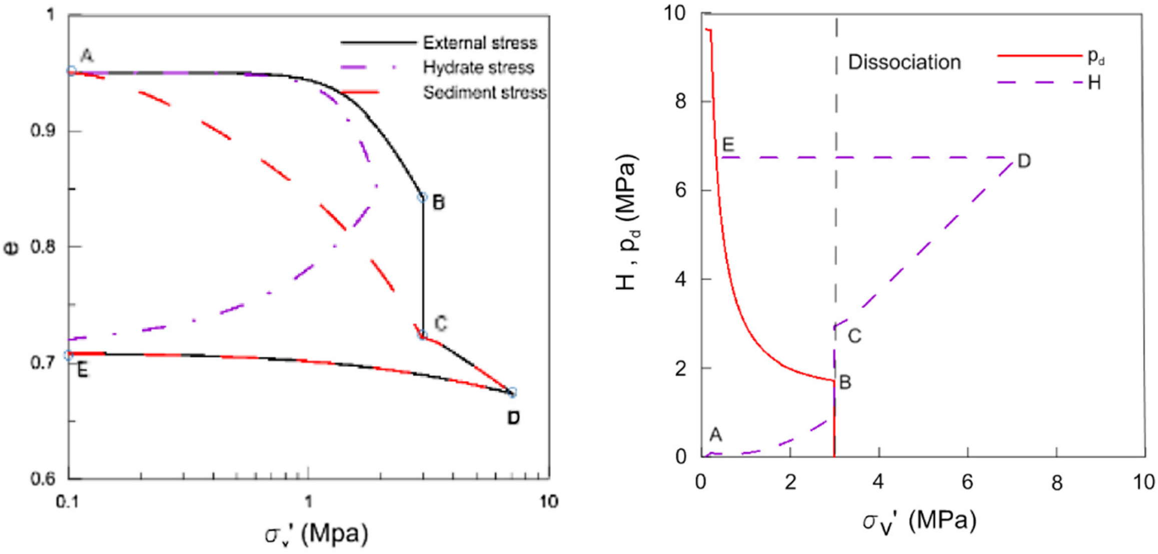

(a)

(b)

Fig. 17. Additional modeling information for the test related to core 10P: (a) vertical stresses computed by the model during loading and (b) hardening variables.

5. Conclusions

A constitutive model for hydrate bearing sediments is presented in this paper. Experimental observations have shown that the presence of hydrates impacts on different aspects of sediment behavior, amongst others: stiffenss, peak stress, softening behavior and dilation. It has been observed that these features of soil behavior depend on hydrate saturation as well. Hydrates also contribute to the mechanical stability of the sediment. Furthermore, during dissociation important changes in the mechanical behavior of HBS and soil structure have been observed. The model proposed in this work encompasses different inelastic mechanisms to describe these complex features of HBS behavior. The concept of stress partition was incorporated into the model to estimate the mechanical contribution associated with hydrates and soil skeleton at different stages of loading and hydrate dissociation. A damage model was adopted to describe the behavior of hydrate during loading, while the HISS elastoplastic model was selected for the sediment skeleton. The HISS model is a versatile mechanical constitutive law based on critical state soil mechanics. The proposed framework also incorporates sub-loading and hydrate enhancement mechanisms.

Information from several mechanical tests recently published is selected to study the model capabilities. The experiments were chosen to cover the most relevant conditions related to HBS behavior. Hydrate soil specimens covering a wide range of hydrate saturations were considered in the analyses. The effect of hydrate morphology and confinement on the mechanical behavior of HBS is also investigated in this work. Particularly attention was paid to the study of the mechanical behavior of HBS during hydrate dissociation under loading. In the cases in which there was enough experimental data, some tests were used for determining the parameters and the other ones were left apart for model validation. The model performance during all of these conditions was very satisfactory. The proposed geomechanical model was capable of capturing not only the main trends and features of sediment observed in the different tests, but also to reproduce very closely the experimental observations in most of the analyzed cases. The enhancement of sediment strength, stiffenss and dilation were well reproduced by the model. The ability of the proposed approach to simulate the volumetric soil collapse compression observed during hydrate dissociation at constant stresses is particularly remarkable. A contribution of this work is the modeling of HBS during dissociation. This model has also assisted to interpret how sediment and hydrates contribute to the mechanical behavior of HBS and how these contributions evolve during loading and hydration dissociation.

Acknowledgements

The authors would like to acknowledge the financial support from NETL (National Energy Technology Laboratory), DOE, USA, through Award No.: DE-FE0013889. The authors would like to gratefully acknowledge Dr. Ajay Shastri for his involvement in the initial developments associated with this model and also Miss Maria De La Fuente for the fruitful discussions.

References

[1] Collett TS. Energy resource potential of natural gas hydrates. AAPG Bull 2002;86(11):1971–92.
[2] Kvenvolden KA. Potential effects of gas hydrate on human welfare. Proc Natl Acad Sci 1999;96(7):3420–6.
[3] Mahajan D, Taylor CE, Mansoori GA. An introduction to natural gas hydrate/clathrate: the major organic carbon reserve of the Earth. J Petrol Sci Eng 2007;56(1):1–8.
[4] Beaudoin Y, Waite W, Boswell R, Dallimore S. Frozen heat: a UNEP global outlook on methane gas hydrates, vol. 1. Norway: United Nations Environmental Programme, GRID-Arendal; 2014. p. 77.
[5] Miyazaki K, Tenma N, Aoki K, Yamaguchi T. A nonlinear elastic model for triaxial compressive properties of artificial methane-hydrate-bearing sediment samples. Energies 2012;5(10):4057–75.
[6] Kimoto S, Oka F, Fushita T, Fujiwaki M. A chemo-thermo-mechanically coupled numerical simulation of the subsurface ground deformations due to methane hydrate dissociation. Comput Geotech 2007;34(4):216–28.
[7] Klar A, Soga K, Ng M. Coupled deformation–flow analysis for methane hydrate extraction. Geotechnique 2010;60(10):765–76.
[8] Rutqvist J, Moridis GJ. Numerical studies on the geomechanical stability of hydrate-bearing sediments. In: Offshore technology conference: offshore technology conference.
[9] Pinkert S, Grozic J. Prediction of the mechanical response of hydrate-bearing sands. J Geophys Res: Solid Earth 2014;119(6):4695–707.
[10] Pinkert S, Grozic J, Priest J. Strain-softening model for hydrate-bearing sands. Int J Geomech 2015;15(6):04015007.
[11] Lin JS, Seol Y, Choi JH. An SMP critical state model for methane hydrate-bearing sands. Int J Numer Anal Meth Geomech 2015;39(9):969–87.
[12] Sánchez M, Gai X. Geomechanical and numerical modeling of gas hydrate sediments. In: Wuttke, Bauer, Sanchez, editors. 1st International conference on energy geotechnics, Kiel, Germany. Energy geotechnics. CRC Press/Balkema; 2016. p. 19–24.
[13] Sultan N, Garziglia S. Geomechanical constitutive modelling of gas-hydrate-bearing sediments. In: The 7th international conference on gas hydrates (ICGH 2011).
[14] Uchida S, Soga K, Yamamoto K. Critical state soil constitutive model for methane hydrate soil. J Geophys Res: Solid Earth (1978–2012) 2012;117(B3).
[15] Uchida S, Xie XG, Leung YF. Role of critical state framework in understanding geomechanical behavior of methane hydrate-bearing sediments. J Geophys Res: Solid Earth 2016;121(8):5580–95.
[16] Gai X, Sánchez M. A geomechanical model for gas hydrate bearing sediments. In: Themed issue: XV panamerican conference on soil mechanics and geotechnical engineering, Buenos Aires, Argentina, Environmental geotechnics (in press). http://dx.doi.org/10.1680/jenge.16.00008.
[17] Jiang M, Chen H, Tapias M, Arroyo M, Fang R. Study of mechanical behavior and strain localization of methane hydrate bearing sediments with different saturations by a new DEM model. Comput Geotech 2014;57:122–38.
[18] Jiang M, Zhu F, Utili S. Investigation into the effect of backpressure on the mechanical behavior of methane-hydrate-bearing sediments via DEM analyses. Comput Geotech 2015;69:551–63.
[19] Liu F, Jiang M, Zhu F. Discrete element analysis of uplift and lateral capacity of a single pile in methane hydrate bearing sediments. Comput Geotech 2014;62:61–76.
[20] Shen J, Chiu C, Ng CW, Lei G, Xu J. A state-dependent critical state model for methane hydrate-bearing sand. Comput Geotech 2016;75:1–11.
[21] Shen Z, Jiang M, Thornton C. DEM simulation of bonded granular material. Part I: contact model and application to cemented sand. Comput Geotech 2016;75:192–209.
[22] Yu Y, Cheng YP, Xu X, Soga K. Discrete element modelling of methane hydrate soil sediments using elongated soil particles. Comput Geotech 2016;80:397–409.
[23] Shen Z, Jiang M. DEM simulation of bonded granular material. Part II: extension to grain-coating type methane hydrate bearing sand. Comput Geotech 2016;75:225–43.
[24] Duncan JM, Chang C-Y. Nonlinear analysis of stress and strain in soils. J Soil Mech Found Div 1970;96(5):1629–53.
[25] Miyazaki K, Masui A, Sakamoto Y, Aoki K, Tenma N, Yamaguchi T. Triaxial compressive properties of artificial methane-hydrate-bearing sediment. J Geophys Res: Solid Earth (1978–2012) 2011;116(B6).
[26] Pinkert S. Rowe's stress-dilatancy theory for hydrate-bearing sand. Int J Geomech 2016. 06016008.
[27] Rowe PW. The stress-dilatancy relation for static equilibrium of an assembly of particles in contact. Proc Roy Soc Lond A: Math Phys Eng Sci 1962:500–27 [The Royal Society].
[28] Masui A, Miyazaki K, Haneda H, Ogata Y, Aoki K. Mechanical characteristics of natural and artificial gas hydrate bearing sediments. In: Proceedings of the 6th international conference on gas hydrates, Vancouver, Canada: ICGH. p. 6–10.
[29] Masui A, Haneda H, Ogata Y, Aoki K. Effects of methane hydrate formation on shear strength of synthetic methane hydrate sediments. In: The fifteenth international offshore and polar engineering conference. International Society of Offshore and Polar Engineers.
[30] Carol I, Rizzi E, Willam K. On the formulation of anisotropic elastic degradation. I. Theory based on a pseudo-logarithmic damage tensor rate. Int J Solids Struct 2001;38(4):491–518.
[31] Fernandez A, Santamarina J. Effect of cementation on the small-strain parameters of sands. Can Geotech J 2001;38(1):191–9.
[32] Pinyol Puigmartí NM, Vaunat J, Alonso Pérez de Agreda E. A constitutive model for soft clayey rocks that includes weathering effects. Geotechnique 2007;57(2):137–51.
[33] Vaunat J, Gens A. Bond degradation and irreversible strains in soft argillaceous rock. In: Proceedings of the 12th Panamerican conference on soil mechanics and geotechnical engineering.
[34] Desai C. Letter to editor single surface yield and potential function plasticity models: a review. Comput Geotech 1989;7(4):319–33.
[35] Desai C, Somasundaram S, Frantziskonis G. A hierarchical approach for constitutive modelling of geologic materials. Int J Numer Anal Meth Geomech 1986;10(3):225–57.
[36] Desai CS. Mechanics of materials and interfaces: the disturbed state concept. CRC Press; 2000.
[37] Hyodo M, Li Y, Yoneda J, Nakata Y, Yoshimoto N, Nishimura A. Effects of dissociation on the shear strength and deformation behavior of methane hydrate-bearing sediments. Mar Pet Geol 2014;51:52–62.
[38] Hyodo M, Nakata Y, Yoshimoto N, Ebinuma T. Basic research on the mechanical behavior of methane hydrate-sediments mixture. Soils Found 2005;45(1):75–85.
[39] Hyodo M, Yoneda J, Yoshimoto N, Nakata Y. Mechanical and dissociation properties of methane hydrate-bearing sand in deep seabed. Soils Found 2013;53(2):299–314.
[40] Li Y-h, Song Y-c, Yu F, Liu W-g, Zhao J-f. Experimental study on mechanical properties of gas hydrate-bearing sediments using kaolin clay. China Ocean Eng 2011;25:113–22.
[41] Miyazaki K, Masui A, Tenma N, Ogata Y, Aoki K, Yamaguchi T, et al. Study on mechanical behavior for methane hydrate sediment based on constant strain-rate test and unloading-reloading test under triaxial compression. Int J Offshore Polar Eng 2010;20(01).
[42] Yun TS, Santamarina JC, Ruppel C. Mechanical properties of sand, silt, and clay containing tetrahydrofuran hydrate. J Geophys Res: Solid Earth (1978–2012) 2007;112(B4).
[43] Zhang X-H, Lu X-B, Zhang L-M, Wang S-Y, Li Q-P. Experimental study on mechanical properties of methane-hydrate-bearing sediments. Acta Mech Sin 2012;28(5):1356–66.
[44] Soga K, Lee S, Ng M, Klar A. Characterisation and engineering properties of methane hydrate soils. Charact Eng Prop Nat Soils 2006:2591–642.
[45] Waite WF, Santamarina JC, Cortes DD, Dugan B, Espinoza D, Germaine J, et al. Physical properties of hydrate-bearing sediments. Rev Geophys 2009;47(4).
[46] Aman ZM, Leith WJ, Grasso GA, Sloan ED, Sum AK, Koh CA. Adhesion force between cyclopentane hydrate and mineral surfaces. Langmuir 2013;29(50):15551–7.
[47] Clayton C, Priest J, Rees E. The effects of hydrate cement on the stiffness of some sands. Géotechnique 2010;60(6):435–45.

[48] Miranda CR, Matsuoka T. First-principles study on mechanical properties of CH_4 hydrate. In: Proceedings of the 6th international conference on gas hydrates, Vancouver, Canada.

[49] Dvorkin J, Uden R. Seismic wave attenuation in a methane hydrate reservoir. Lead Edge 2004;23(8):730–2.

[50] Berge LI, Jacobsen KA, Solstad A. Measured acoustic wave velocities of R11 (CCl3F) hydrate samples with and without sand as a function of hydrate concentration. J Geophys Res: Solid Earth (1978–2012) 1999;104 (B7):15415–24.

[51] Yun T, Francisca F, Santamarina J, Ruppel C. Compressional and shear wave velocities in uncemented sediment containing gas hydrate. Geophys Res Lett 2005;32(10).

[52] Yun TS, Narsilio GA, Santamarina JC. Physical characterization of core samples recovered from Gulf of Mexico. Mar Pet Geol 2006;23(9):893–900.

[53] Helgerud M, Dvorkin J, Nur A, Sakai A, Collett T. Elastic-wave velocity in marine sediments with gas hydrates: effective medium modeling. Geophys Res Lett 1999;26(13):2021–4.

[54] Dai J, Xu H, Snyder F, Dutta N. Detection and estimation of gas hydrates using rock physics and seismic inversion: examples from the northern deepwater Gulf of Mexico. Lead Edge 2004;23(1):60–6.

[55] Santamarina JC, Dai S, Terzariol M, Jang J, Waite WF, Winters WJ, et al. Hydro-bio-geomechanical properties of hydrate-bearing sediments from Nankai Trough. Mar Pet Geol 2015;66:434–50.

[56] Santamarina JC, Dai S, Jang J, Terzariol M. Pressure core characterization tools for hydrate-bearing sediments. Sci Drill 2012;14(4).

[57] Chaouachi M, Falenty A, Sell K, Enzmann F, Kersten M, Haberthür D, et al. Microstructural evolution of gas hydrates in sedimentary matrices observed with synchrotron X-ray computed tomographic microscopy. Geochem Geophys Geosyst 2015;16(6):1711–22.

[58] Kachanov L, Krajcinovic D. Introduction to continuum damage mechanics. Springer Science & Business Media; 2013.

[59] Hashiguchi K. Elasto-plastic constitutive laws of granular materials, constitutive equations of soils. In: Proc spec session 9 of 9th int ICSMFE. p. 73–82.

[60] Hashiguchi K. Subloading surface model in unconventional plasticity. Int J Solids Struct 1989;25(8):917–45.

[61] Sloan SW. Substepping schemes for the numerical integration of elastoplastic stress–strain relations. Int J Numer Meth Eng 1987;24(5):893–911.

[62] Gai X. Geomechanical modeling of gas hydrate bearing sediment using an advanced coupled approach. Texas A&M University; 2016.

[63] Yoneda J, Masui A, Konno Y, Jin Y, Egawa K, Kida M, et al. Mechanical properties of hydrate-bearing turbidite reservoir in the first gas production test site of the Eastern Nankai Trough. Mar Pet Geol 2015;66:471–86.

[64] Priest JA, Rees EV, Clayton CR. Influence of gas hydrate morphology on the seismic velocities of sands. J Geophys Res: Solid Earth 2009;114(B11).